

GENERAL ARTICLE

Mutation in *Eftud2* causes craniofacial defects in mice via mis-splicing of *Mdm2* and increased P53

Marie-Claude Beauchamp¹, Anissa Djedid², Eric Bareke², Fjodor Merkuri³, Rachel Aber⁴, Annie S. Tam^{5,6}, Matthew A. Lines⁷, Kym M. Boycott⁷, Peter C. Stirling^{5,6}, Jennifer L. Fish³, Jacek Majewski² and Loydie A. Jerome-Majewska^{1,2,4,8,*}

¹ Research Institute of the McGill University Health Centre at Glen Site, Montreal, QC H4A 3J1, Canada,

²Department of Human Genetics, McGill University, Montreal, QC H3A 0G1, Canada, ³Department of Biological Sciences, University of Massachusetts Lowell, Lowell, MA 01854, USA, ⁴Department of Anatomy and Cell Biology, McGill University, Montreal, QC H3A 2B2, Canada, ⁵Terry Fox Laboratory, British Columbia Cancer Agency, Vancouver, BC V5Z 1L3, Canada, ⁶Department of Medical Genetics, University of British Columbia, Vancouver, BC V6H 3N1, Canada, ⁷CHEO Research Institute, University of Ottawa, Ottawa, ON K1H 8L1, Canada and ⁸Department of Pediatrics, McGill University, Montreal, QC H4A 3J1, Canada

*To whom correspondence should be addressed. Tel: (514) 934-1934 ex 23279; Fax: 514-933-4149; Email: loydie.majewska@mcgill.ca

Abstract

EFTUD2 is mutated in patients with mandibulofacial dysostosis with microcephaly (MFDM). We generated a mutant mouse line with conditional mutation in *Eftud2* and used *Wnt1-Cre2* to delete it in neural crest cells. Homozygous deletion of *Eftud2* causes brain and craniofacial malformations, affecting the same precursors as in MFDM patients. RNAseq analysis of embryonic heads revealed a significant increase in exon skipping and increased levels of an alternatively spliced *Mdm2* transcript lacking exon 3. Exon skipping in *Mdm2* was also increased in O9-1 mouse neural crest cells after siRNA knock-down of *Eftud2* and in MFDM patient cells. Moreover, we found increased nuclear P53, higher expression of P53-target genes and increased cell death. Finally, overactivation of the P53 pathway in *Eftud2* knockdown cells was attenuated by overexpression of non-spliced *Mdm2*, and craniofacial development was improved when *Eftud2*-mutant embryos were treated with Pifithrin- α , an inhibitor of P53. Thus, our work indicates that the P53-pathway can be targeted to prevent craniofacial abnormalities and shows a previously unknown role for alternative splicing of *Mdm2* in the etiology of MFDM.

Introduction

Splicing is the essential mechanism via which the coding exons of pre-mRNAs are joined and the intervening non-coding sequences are removed. Splicing also contributes to proteomic diversity and regulates mRNA levels via alternative splicing, the process of inclusion and skipping of 'alternative' exons (1–3). The major spliceosome, a ribonucleoprotein complex that

regulates and performs the splicing reaction, catalyzes 99% of RNA splicing reactions in human (4). On the other hand, the minor or U12-dependent spliceosome is only responsible for splicing of approximately 700 minor introns in 666 genes (5).

The major spliceosome is composed of U1, U2, U5 and U4/U6 small nuclear ribonucleoproteins (snRNPs) named for their core associated small RNAs (snRNAs). The minor or U12-dependent

spliceosome consists of U11, U12, U5 and U4atac/U6atac snRNAs and shares all but 7 proteins with the major spliceosome (6). The sequential steps in splicing include recognition of a 5'-splice site via the U1/U11 snRNP, binding of U2/U12 snRNP to the branch site on the intron, recruitment of the pre-assembled U4/U6.U5 or U4atac/U6atac/U5 snRNPs, cleavage of the intervening intron, and ligation of the two exons. This process is ubiquitous and yet, mutations in components of the spliceosome can result in tissue-specific abnormalities ranging from retinitis pigmentosa to craniofacial malformations (7–10).

Mutations in EFTUD2, a GTPase and a core component of the U5 snRNP, are responsible for mandibulofacial dysostosis with microcephaly (MFDM; OMIM#610536). MFDM patients exhibit a variety of clinical phenotypes of which the most common are: microcephaly, developmental delay, mandibular and malar hypoplasia, as well as external ear anomalies. Amongst the approximately 100 individuals with MFDM reported to date, 86 distinct heterozygous EFTUD2 mutations have been found, including: deletions/duplications, frameshift, nonsense, splice site and missense (11–24). Most of these mutations are *de novo*, although approximately 19% are inherited from an affected parent. Mutations are distributed along the length of the gene, and are presumed to result in a loss of function since no genotype–phenotype correlation is found.

Our aim is to uncover the etiology of craniofacial malformations in MFDM using mutant mouse models of *Eftud2*. However, despite a 30% reduction of *Eftud2* mRNA and protein levels, mice with constitutive heterozygous deletion of exon 2 of *Eftud2* (*Eftud2*^{+/-}) are viable and fertile, and exhibit no craniofacial malformations (25). Additionally, RNA sequencing revealed no significant splicing changes in *Eftud2*^{+/-} embryos when compared with wild-type littermates. Furthermore, homozygous *Eftud2* (*Eftud2*^{-/-}) mutant blastocysts failed to implant, precluding analysis of the role of *Eftud2* during craniofacial development (25). These and other past studies confirmed that *Eftud2* is an essential gene, but its role in neural crest cells, the precursors of bones and cartilages affected in the head and face of MFDM patients, has not been examined (7,17,26,27). Therefore, we generated a conditional *Eftud2* knock-out mouse (*Eftud2*^{loxP/+}) in which exon 2 is flanked by loxP sequences to study the role of *Eftud2* during craniofacial development. In the present study, we evaluated the effect of deletion of exon 2 of *Eftud2* in the developing brain and neural crest cells using the *Wnt1-Cre2* transgenic mouse line. We show that embryos with homozygous mutation of *Eftud2* in the neural crest cells have brain and midface abnormalities and faithfully modeled MFDM. Malformations were associated with alternative splicing of *Mdm2* and increased P53 protein and activity. Knockdown of *Eftud2* increased cell death, and mutant embryos treated with Pifithrin- α , a small molecule inhibitor of P53 (28), showed significant rescue of craniofacial and brain defects. Altogether our data indicate that loss of EFTUD2 in neural crest cells results in differential splicing of *Mdm2* and triggers a P53-associated stress response that leads to craniofacial defects.

Results

Homozygous mutation of *Eftud2* in neural crest cells causes craniofacial malformations and embryonic lethality

To characterize the role of *Eftud2* in neural crest cells, we used *Wnt1-Cre2* transgenic mice (29). Since *Eftud2*^{+/-} embryos were morphologically and molecularly indistinguishable from

wild-type embryos (25), matings of *Eftud2*^{loxP/+}; *Wnt1-Cre2*^{tg/+} or *Eftud2*^{+/-}; *Wnt1-Cre2*^{tg/+} mice to *Eftud2*^{loxP/loxP} mice were used to generate homozygous mutant embryos for analysis. From E8.5 to E17.5, embryos of all genotypes were found at the expected Mendelian ratio (Supplementary Material, Table S1).

Between E8.5 and E10.5, all embryos including homozygous mutants were alive as assessed by the presence of a heart beat. However at E9.5, neural crest cell-specific *Eftud2* homozygous mutant embryos (*Eftud2*^{loxP/-}; *Wnt1-Cre2*^{tg/+} or *Eftud2*^{loxP/loxP}; *Wnt1-Cre2*^{tg/+}) were morphologically abnormal when compared with their control litter mates (*Eftud2*^{loxP/+}; *Wnt1-Cre2*^{tg/+}, or *Eftud2*^{loxP/+}; Supplementary Material, Table S2). Homozygous mutant embryos exhibited hypoplasia of the midbrain, the frontonasal prominence, and of the first and second pharyngeal arches when compared with somite-matched controls (Fig. 1A–C).

Between E11.5 and E17.5, neural crest cell-specific *Eftud2* homozygous mutant embryos showed severe malformations in the head region. At E11.5, 38% of mutant embryos were recovered dead with no heart beat (3/8). The midbrain region was virtually absent in all neural crest cell-specific *Eftud2* homozygous mutants. Brain malformations are most likely a consequence of deletion of *Eftud2* in the midbrain region, where *Wnt1-Cre2* is expressed at E8.5 (29). The frontonasal prominence was abnormally shaped, the maxillary and mandibular processes were present but very small (arrowhead), and all had coloboma. Additionally, three of the eight had an open neural tube (star; Fig. 1E).

At E14.5, most neural crest cell-specific *Eftud2* homozygous mutant embryos were dead or resorbed (9/13), and live embryos had exencephaly ($n = 4/4$; Fig. 1F). Among these, eyes could be seen in only one embryo as they were covered by brain tissue in the remaining three. The pinnae or the external ear was not found in any mutant embryos. The frontonasal, maxillary and mandibular regions were hypoplastic and the maxillary process was cleft in all embryos. A hypoplastic tongue was found protruding from the oropharyngeal region (Fig. 1F). At E16.5 and E17.5, no neural crest cell-specific *Eftud2* homozygous mutant embryos were found alive (Supplementary Material, Table S2). In fact, 4/5 were resorbed with little to no embryonic tissue. Only one dead mutant was recovered at E17.5. As shown in Figure 1G, the nasal and the maxillary processes were hypoplastic and much shorter than the mandibular process. The external ear did not form and the skull was almost absent, leaving the brain exposed. Taken together, these data indicate that during craniofacial development, *Eftud2* is essential in neural crest cells for formation of structures derived from these cells.

Death of neural crest cell-specific *Eftud2* homozygous mutant embryos by E14.5 precluded an analysis of craniofacial bone development. Hence, we used Alcian blue staining to examine craniofacial cartilage of E14.5 embryos. This analysis revealed an absence or hypoplasia of cartilages in the head of neural crest cell-specific *Eftud2* homozygous mutant embryos (Fig. 2A and Supplementary Material, Fig. S1). Neural crest derived cartilages which will form the chondrocranium or the base of the skull, and the mid and lower portions of the face, were hypoplastic or missing. Cartilages found in the head of control embryos (stars in Fig. 2B) and missing in mutants included: the alar temporalis cartilage (A), the basitrabecular process (B), the orbital cartilage (O), the trabecular cartilage (T) and the paranasal cartilage (PN). Also, one embryo had an absence whereas another one had a reduction of Meckel's cartilage (M), the precursor of the lower jaw (Fig. 2A, B and Supplementary Material, Fig. S1). In contrast, cartilages in the chondrocranium that were derived from

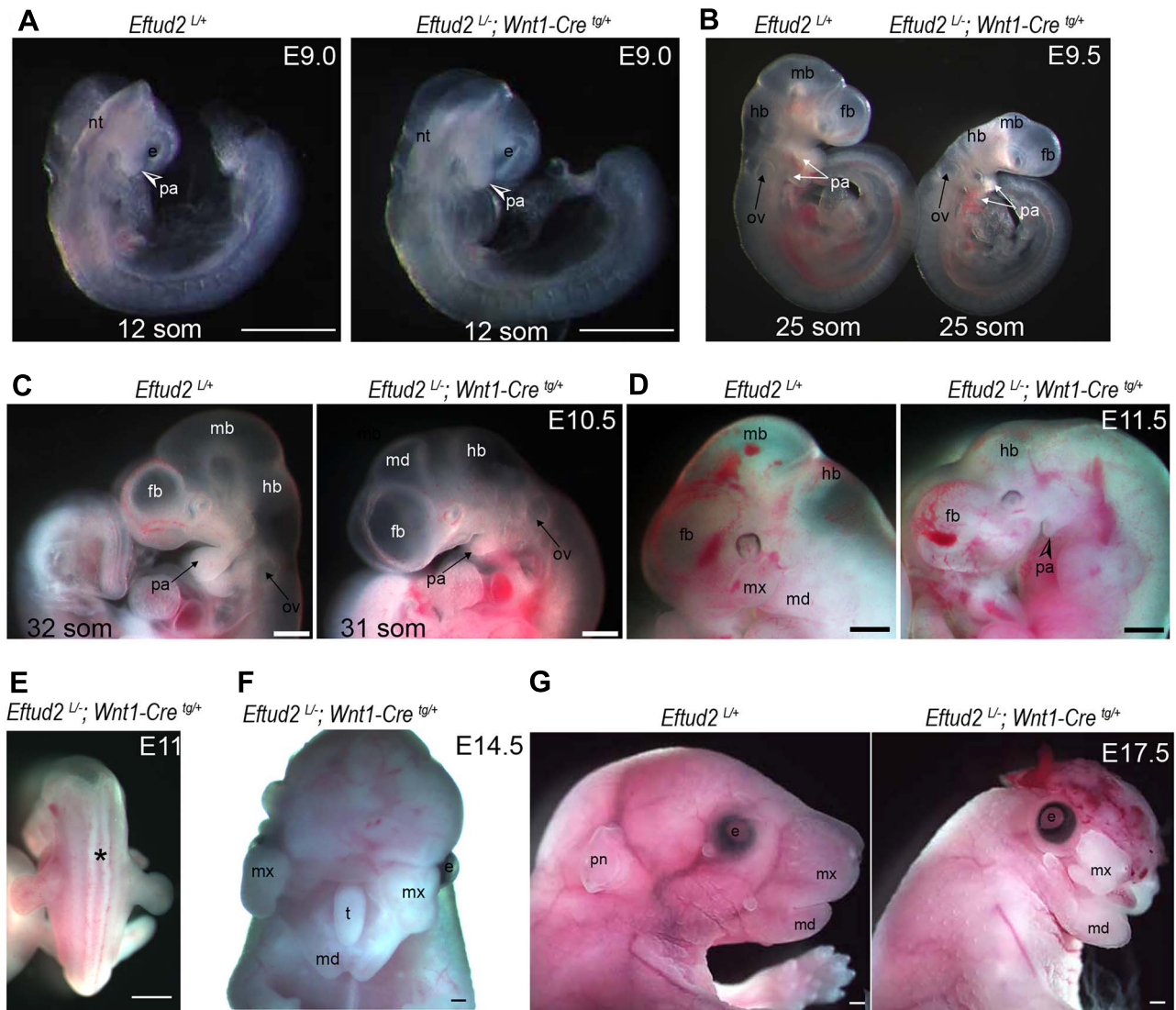


Figure 1. Homozygous mutation of *Eftud2* in neural crest cells causes craniofacial malformations. (A) *Eftud2^{loxP/-}; Wnt1-Cre^{tg/+}* mutant embryos are not distinguishable from controls at E9.0. (B) At E9.5, (C) E10.5 and (D) E11.5, *Eftud2^{loxP/-}; Wnt1-Cre^{tg/+}* mutant embryos exhibit hypoplasia of the midbrain (mb) and pharyngeal arches (pa). (E) The star indicates the open neural tube in an E11.5 mutant embryo. (F) Embryos found alive at E14.5 had exencephaly and an absence of snout and head structures. A frontal view of an E14.5 mutant embryo showing a protruding tongue from the oropharyngeal region, a cleft maxillary process and the fused mandibular process. (G) Images of live wild type (left) and dead mutant (right) embryos at E17.5. Mutant image shows a hypoplastic lower jaw, cleft maxillary process, missing head structures and absence of eyelid closure. nt: neural tube, pa: pharyngeal arch, hb: hindbrain, mb: midbrain, fb: forebrain, ov: otic vesicle, mx: maxillary, md: mandibular prominence, pn: pinna, t: tongue, e: eye. Scale bar = 500 μ m.

mesoderm were present but reduced in size. Hypoplastic cartilages included: the occipital arch cartilage (OA), the parachordal cartilage (P) and the hypochiasmatic cartilage (Y). Middle ear ossicles: the incus, malleus and stapes were not found, and the inner ear was abnormal in both embryos. Identifiable cartilages of the inner ear (Fig. 2B) were the cochlear part of the auditory capsule (CO) and the canicular part of auditory capsule (CA), both of which were abnormally shaped and reduced in size.

Hematoxylin and eosin staining of the remaining two live embryos confirmed variable levels of hypoplasia and aplasia in the craniofacial region (Fig. 2C and D). In addition, the outflow tract failed to be divided into the aorta and pulmonary artery,

indicating that persistent truncus arteriosus may contribute to the death of neural crest cell-specific *Eftud2* homozygous mutant embryos (Fig. 2E). Aside from this, organogenesis appeared normal in mutant embryos.

Abnormal trigeminal cranial ganglia formation in neural crest cell-specific *Eftud2* homozygous mutant embryos

In addition to the cartilage and skeletal elements of the face and head, cranial neural crest cells together with ectodermal

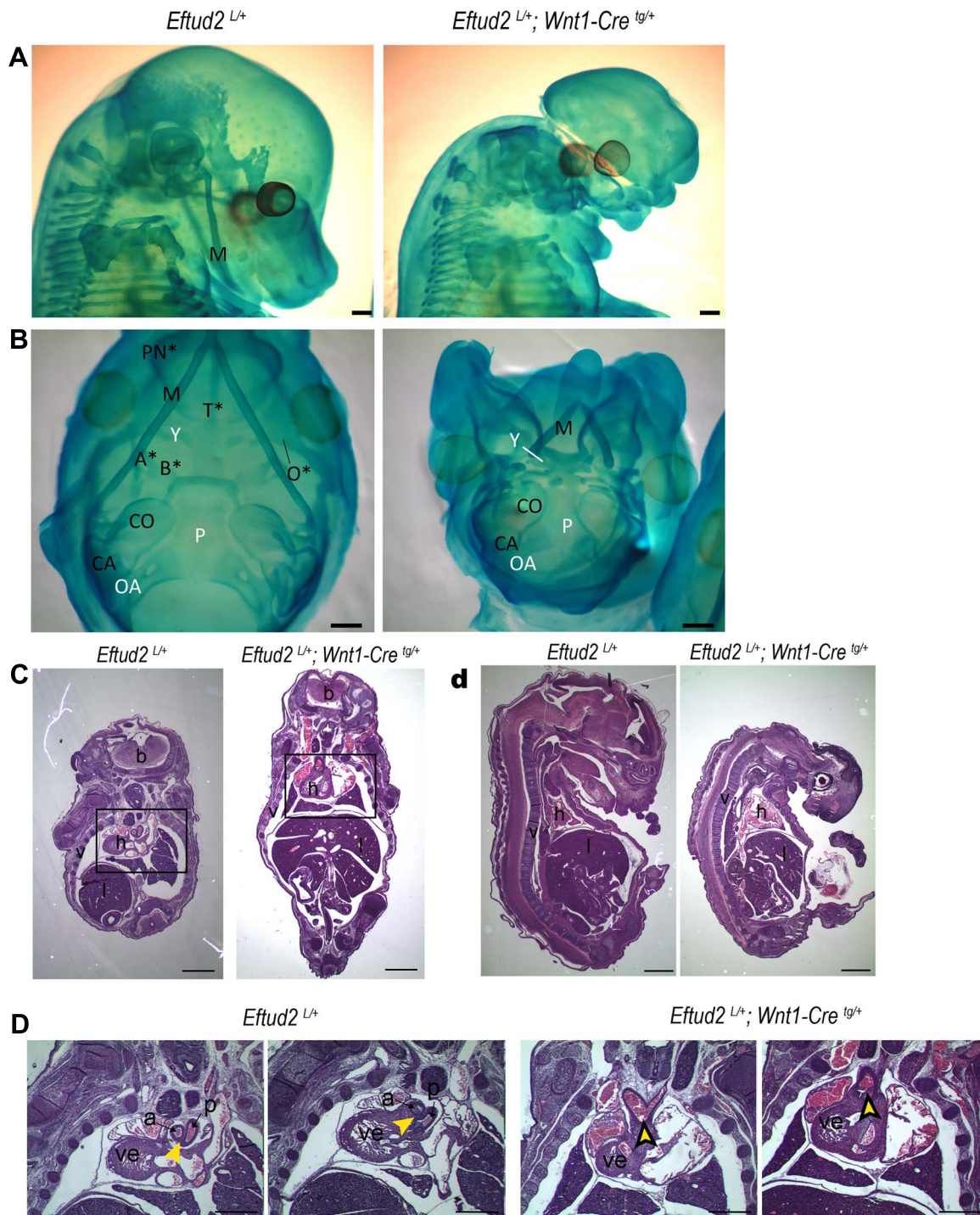


Figure 2. Head and face cartilages are missing or hypoplastic in E14.5 *Eftud2*^{loxP/+}; *Wnt1-Cre2*^{tg/+} mutant embryos. (A) side view of a control (*Eftud2*^{loxP/+}) and *Eftud2*^{loxP/+}; *Wnt1-Cre2*^{tg/+} mutant embryo. Cartilages did not differentiate in the head or face of this mutant embryo. (B) Ventral view of a control and another *Eftud2*^{loxP/+}; *Wnt1-Cre2*^{tg/+} mutant embryo showing a hypoplastic Meckel's cartilage (M) and hypoplasia of the chondrocranium. Structures missing in the mutant are labeled with a star. A: alas temporalis cartilage, B: basitrabecular process, O: orbital cartilage, T: trabecular cartilage, PN: paranasal cartilage, OA: occipital arch cartilage, P: parachordal cartilage, Y: hypochiasmatic cartilage, CO: cochlear part of the auditory capsule, CA: canalicular part of auditory capsule. (C) Frontal and (D) sagittal view of H&E stained sections of control and mutant embryos. v: vertebra, h: heart, l: liver, b: brain. (E) Higher magnification of serial frontal sections showing a single outflow tract in mutant embryo compared with control (open versus full arrowhead) ve: ventricle, a: aorta, p: pulmonary trunk. Scale bar = 500 μm.

placodes, contribute to the formation of the trigeminal (Cranial Nerve; CN V), facial (CN VII), vestibulocochlear (CN VIII), glosopharyngeal (CN IX) and vagus nerves (CN X). To assess the development of the sensory ganglia, we examined expression of

the transcription factor *Sox10*, a key regulator of neural crest-derived peripheral glia, at E9.5. At this stage (n = 2), *Sox10* was expressed in all forming sensory ganglia and in otic vesicles of control embryos. In neural crest cell-specific *Eftud2* homozygous

mutant embryos ($n=3$), *Sox10* expression was reduced in the ganglia, but found in the otic vesicle of all mutant embryos (Supplementary Material, Fig. S2). At E10.5, ($n=4$) expression in CN V and VII/VIII was variable and found in two and four mutant embryos, respectively. Additionally, *Sox10* expression was found in CN IX in two mutant embryos and in dorsal root ganglia of one (star), but not found in CN X of any mutants (Fig. 3A).

Similarly, at E9.5 and E10.5, immunohistochemistry using the pan neurofilament antibody 2H3 revealed abnormally formed cranial sensory ganglia in all mutant embryos ($n=5$). At E9.5, all forming cranio sensory ganglia were distinguishable in controls ($n=2$) whereas in mutants ($n=2$), staining was only found in cranial nerve V and cranial nerve VII (Supplementary Material, Fig. S2). At E10.5 ($n=3$), reduced 2H3 staining was found in CN V and CN VII/VIII, CN IX and CN X in one mutant embryo (Fig. 3B), whereas CN IX and X were hard to detect in two others. Thus, sensory cranial ganglia are formed in neural crest cell-specific *Eftud2* homozygous mutant embryos, however, these ganglia are abnormal.

Eftud2 mutant neural crest cells migrate to the craniofacial region but fail to survive and/or expand

To determine if neural crest cell generation and/or migration were disrupted by mutation of *Eftud2*, we generated embryos expressing the R26R reporter and used X-Gal staining to visualize neural crest cells and their derivatives. Similar to what was previously reported, X-Gal positive cells were also found in the neural plate (30). At E9.0, the region of X-Gal positive neural crest cells in heads of mutant and control embryos analyzed in wholemounts or after cryosection was comparable (Fig. 3C and F). However, at E9.5 and E10.5, wholemount followed by cryosection revealed that regions of X-Gal positive neural crest cells in the frontonasal region and pharyngeal arches of mutant embryos were significantly reduced when compared with controls (Fig. 3D and E and full versus open arrowheads in G and H). Moreover, the post-otic streams of X-Gal positive neural crest cells from the hindbrain to pharyngeal arches 2 and 3 found in control embryos were missing in homozygous mutant embryos (full versus open arrowheads, Fig. 3D and E). Thus, we concluded that either fewer *Eftud2* mutant neural crest cells are generated or fewer of these cells migrate and colonize the developing craniofacial region, either due to a block in survival, expansion and/or differentiation.

Eftud2 mutant neural crest cells have increased levels of cell death

To determine if proliferation is perturbed in E9.0 neural crest cell-specific *Eftud2* homozygous mutant embryos, immunofluorescence was used to stain for phospho-histone H3 (PH3) to label cells in mitosis. The number of PH3 positive cells found in mutants ($n=4$) and controls ($n=5$) was not significantly different between the two groups (Fig. 4A and B). We next examined apoptosis at E9.0 using TUNEL assay to label apoptotic nuclei. Though more TUNEL positive nuclei were found in mutants ($n=4$) when compared with controls ($n=5$), this difference was not statistically significant (Fig. 4C and D). At E9.5, a significant increase in TUNEL positive cells was found in the craniofacial region of in neural crest cell-specific *Eftud2* homozygous mutant embryos ($n=4$) when compared with wild-type controls ($n=3$; Fig. 4E and F). These findings indicate that apoptosis contributes to the reduced number of *Eftud2* mutant neural crest cells found from E9.5 to E10.5.

To further test if reducing levels of *Eftud2* increases apoptosis of neural crest cells, O9-1 cells transfected with *Eftud2* siRNA or control siRNA were stained with Annexin V. A significant increase in Annexin V staining intensity was found in cells with knockdown of *Eftud2*, when compared with controls. These data indicate that cultured neural crest cells with reduced levels of *Eftud2* undergo apoptosis (Fig. 4G).

Altered transcriptional landscape in *Eftud2* homozygous neural crest mutants

EFTUD2 is a core component of the spliceosome, so we next sought to investigate whether its absence results in detectable defects or alterations in pre-mRNA splicing. We used ribo-depleted RNA isolated from the craniofacial regions of E9.0 and E9.5 neural crest cell-specific *Eftud2* homozygous mutant embryos (*Eftud2*^{loxP/-}; *Wnt1-Cre2^{tg/+}*) and controls (*Eftud2*^{loxP/+}; *Wnt1-Cre2^{tg/+}*) for RNAseq (see Materials and Methods and Supplementary Material, Tables S6 and S7). We then used the rMATS computational package to identify splicing differences between *Eftud2* homozygous mutants and controls, including skipped exons, retained introns, the use of alternative 5' or 3' splice sites and mutually exclusive exons. We expected the differences that most directly reflect the effects of *Eftud2* deletion to be present at E9.0 (before the onset of first phenotypic differences), whereas differences at E9.5 may reflect a combination of both direct and secondary effects resulting from altered development.

Exon skipping was the most frequent type of differential alternative splicing event with 567 (E9.0) and 380 (E9.5) differential exon skipping events (FDR < 0.05; Fig. 5A and Supplementary Material, Fig. S3A). The most significant detected event was the skipping of exon 2 of *Eftud2*; while this is not an actual alternative splicing event, but the result of the targeted deletion, it serves as a convenient positive control indicating the validity of the analysis. Exclusion of exon 2 of *Eftud2* from the RNA sequencing data also allows us to estimate the fraction of neural crest cells present within the mutant and controls craniofacial regions (see Materials and Methods) to be 21% at E9.0. At E9.5, this proportion increases to 45% in the control embryos, but falls to 15% in the mutants, providing independent confirmation for the inability of *Eftud2* mutant neural crest cells to survive and/or expand (Fig. 5F). Among legitimate skipped exon events, there was a clear and significant tendency for increased exon skipping in mutants at both stages (Fig. 5A and Supplementary Material, Fig. S3A). No difference was found for mutually exclusive exons (data not shown). Among the remaining alternative splicing differences, there was a slight significant preference for the usage of upstream splice sites (alternative 5' and 3' sites) at E9.0, however, this trend was not observed at E9.5 (Fig. 5C, D and Supplementary Material, Fig. S3C, D). Intron inclusion was preferentially decreased in mutants at both stages, but notably the overall number of detected retained introns was small (Fig. 5B and Supplementary Material, Fig. S3B).

Retained introns are traditionally difficult to identify, and to further explore intron retention differences, we used IRFinder (31), an approach specifically designed for this purpose. The most significant differential intron retention events, at both developmental stages, were the 2 introns flanking exon 2 of *Eftud2*; again, although this is not a true splicing difference, it is a positive control validating the approach. We used a nominal P-value < 0.05 as a selection criterion in order to study any tendencies for intron inclusion that may result from *Eftud2* deletion. At stage E9.0, we detected more retained introns in the mutant (436

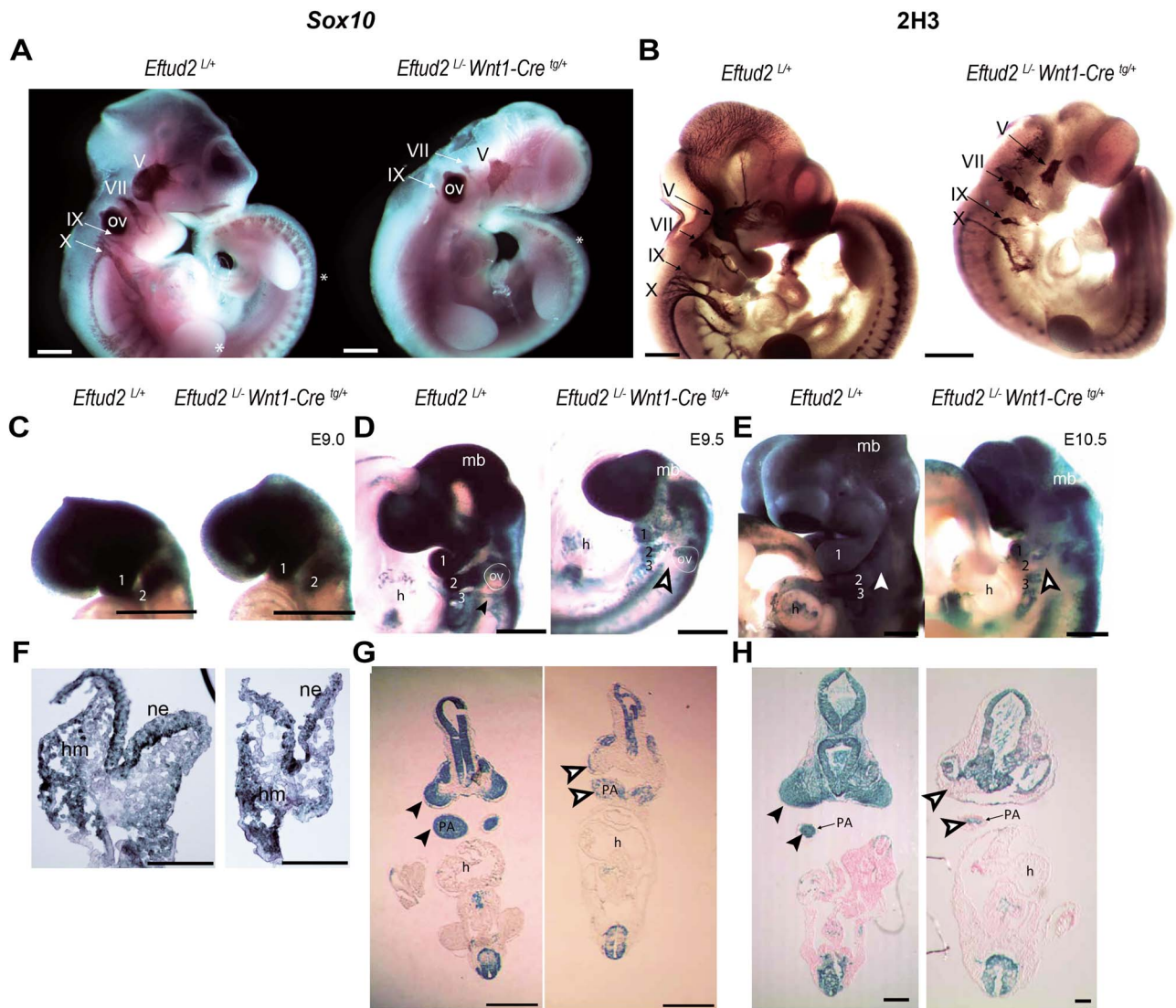


Figure 3. Abnormal trigeminal cranial ganglia formation and reduced neural crest cells in the craniofacial region of *Eftud2*^{loxP/-}; *Wnt1-Cre2*^{tg/+} or *Eftud2*^{loxP/loxP}; *Wnt1-Cre2*^{tg/+} mutant embryos. Cranial nerves V, VII, IX and X can be seen in representative images of control (*Eftud2*^{loxP/+}) and mutant E10.5 embryos (A) after wholemount in-situ hybridization to detect *Sox10* expression (purple), and (B) wholemount IHC staining with 2H3 neurofilament antibody (brown). Representative images of control and mutant embryos showing neural crest cells in the developing craniofacial region (blue) (C) occupy a similar region in E9.0 embryos. (D) At E9.5 and (E) E10.5, the region occupied by neural crest cells in the pharyngeal region of *Eftud2*^{loxP/-}; *Wnt1-Cre2*^{tg/+} mutant embryos is reduced. Post-otic streams of neural crest cells destined for pharyngeal arches 3 and 4 (black arrowhead), were absent in *Eftud2*^{loxP/-}; *Wnt1-Cre2*^{tg/+} mutant embryos (white arrowheads). (F–H) Frontal sections of wholemount stained embryos at (F) E9.0 (G) E9.5 and (H) E10.5. ne: neuroepithelium, hm: head mesenchyme. PA: pharyngeal arch, ov: otic vesicle, h: heart. Scale bar = 500 μ m.

out of 550, $P = 2.4 \times 10^{-45}$). Paradoxically, this tendency was reversed at E9.5 with significantly lower numbers of retained introns in the mutant (238 out of 769, $P = 1.53 \times 10^{-26}$).

To further investigate possible mechanisms through which EFTUD2 may affect splicing, we focused on the most consistent and abundant trend in exon-skipping in the mutants and considered the E9.0 stage, where the contribution of neural crest cells to the head region was comparable in mutants and controls. We compared splice site strength and nucleotide profiles between exons that were preferentially skipped in the mutant (representing the types of splice sites that may be less efficiently recognized in the absence of EFTUD2) to the splice sites that were preferentially included in the mutant (which we believe would represent secondary downstream splicing differences, likely independent of EFTUD2). However, we did not observe any difference in splice sites characteristics (Supplementary

Material, Fig. S4), suggesting that EFTUD2 may not be involved in the process of splice site recognition. To explore this idea further, we asked whether the absence of EFTUD2 may result in more frequent usage of unannotated or cryptic splice sites. Again, we did not detect any difference in unannotated spliced-site usage, suggesting that the absence of EFTUD2 does not result in mis-directing the splicing machinery to atypical splicing signals (Supplementary Material, Fig. S5).

Alternative splicing events could potentially lead to changes in gene expression with the introduction of exons containing premature termination codons (PTC). Therefore, we compared log fold change of transcripts with skipped exons or retained introns. No significant difference was found in the expression level of these genes (Supplementary Material, Fig. S6). Next, we specifically identified those skipped exons events that were predicted to introduce PTCs and asked whether increased PTC

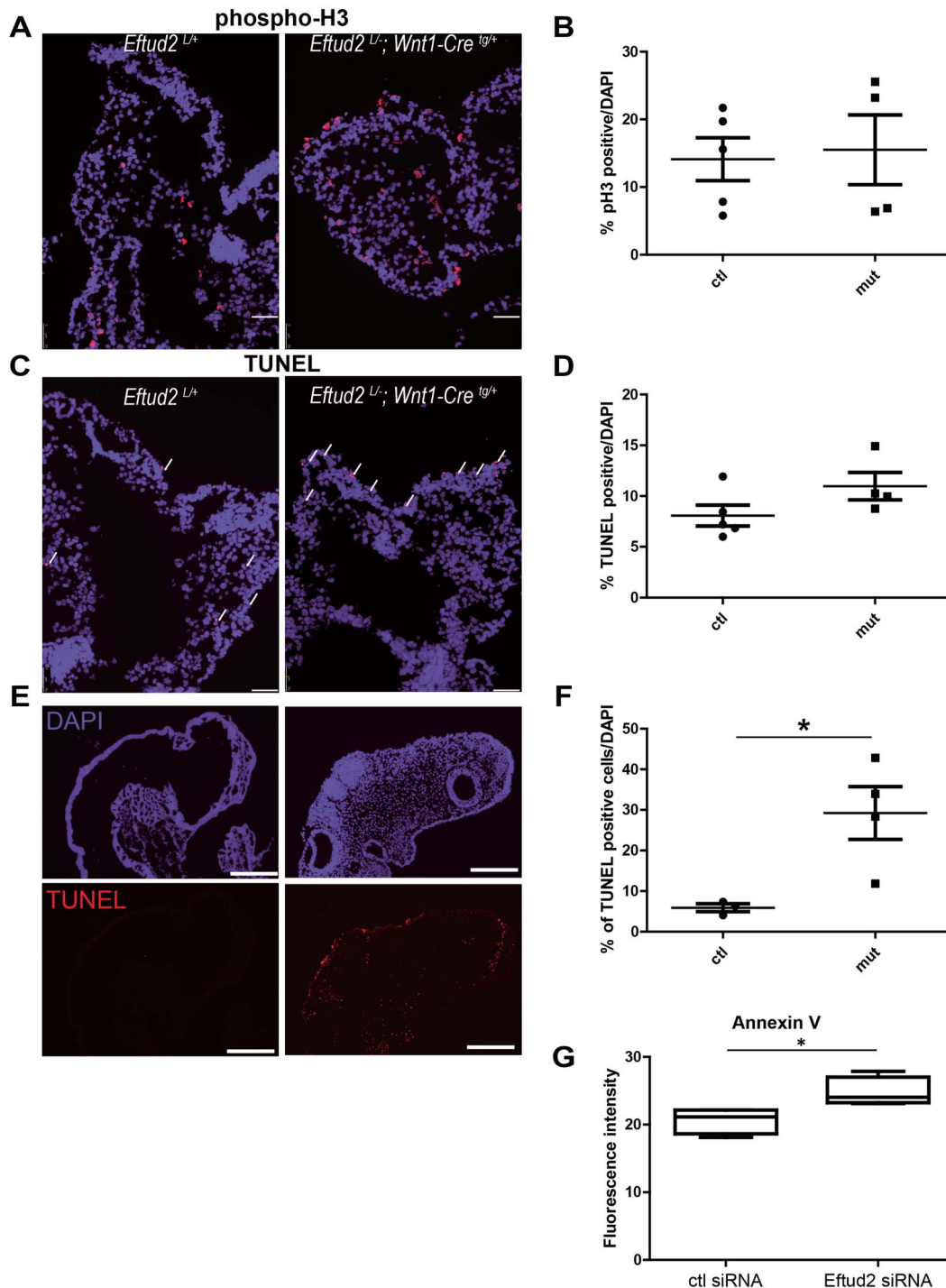


Figure 4. *Eftud2* mutant neural crest cells have increased levels of cell death. (A) Representative images of E9.0 control (*Eftud2^{loxP/+}*) and mutant (*Eftud2^{loxP/-}; Wnt1-Cre^{tg/+}*) embryos showing phospho-histone H3 positive (red) nuclei. Scale bar = 100 μ m. (B) quantification of the % of PH3 stained cells/DAPI. (C) Representative images of E9.0 control and mutant embryos showing TUNEL positive cells (red) indicated by white arrows. Scale bar = 100 μ m. (D) quantification of the % of TUNEL positive cells/DAPI. (E) Representative images of E9.5 control and mutant embryos showing TUNEL positive cells (red) nuclei, DAPI (blue) scale bar = 280 μ m (F) quantification of the % of TUNEL positive cells/DAPI. * $P < 0.05$. (G) Boxplot of Annexin V fluorescence intensity, in arbitrary units, for control ($n = 6$) and knockdown ($n = 4$) 09-1 neural crest cells 24–30 h post-transfection with negative control or *Eftud2* siRNAs, respectively. A Kruskal–Wallis rank sum test was used to determine the significance associated with the difference between the treatment groups (* $P \leq 0.05$).

corresponded to decreased expression of host genes. Among the 82 PTC-causing exons that were significantly more included in mutants than controls, 48 were associated with increased, while 34 were associated with decreased gene expression

(Supplementary Material, Fig. S6). Furthermore, the magnitude of gene expression differences was not different between the genes with increased and decreased expression. Similar analysis of events with retained introns suggest that in heads of

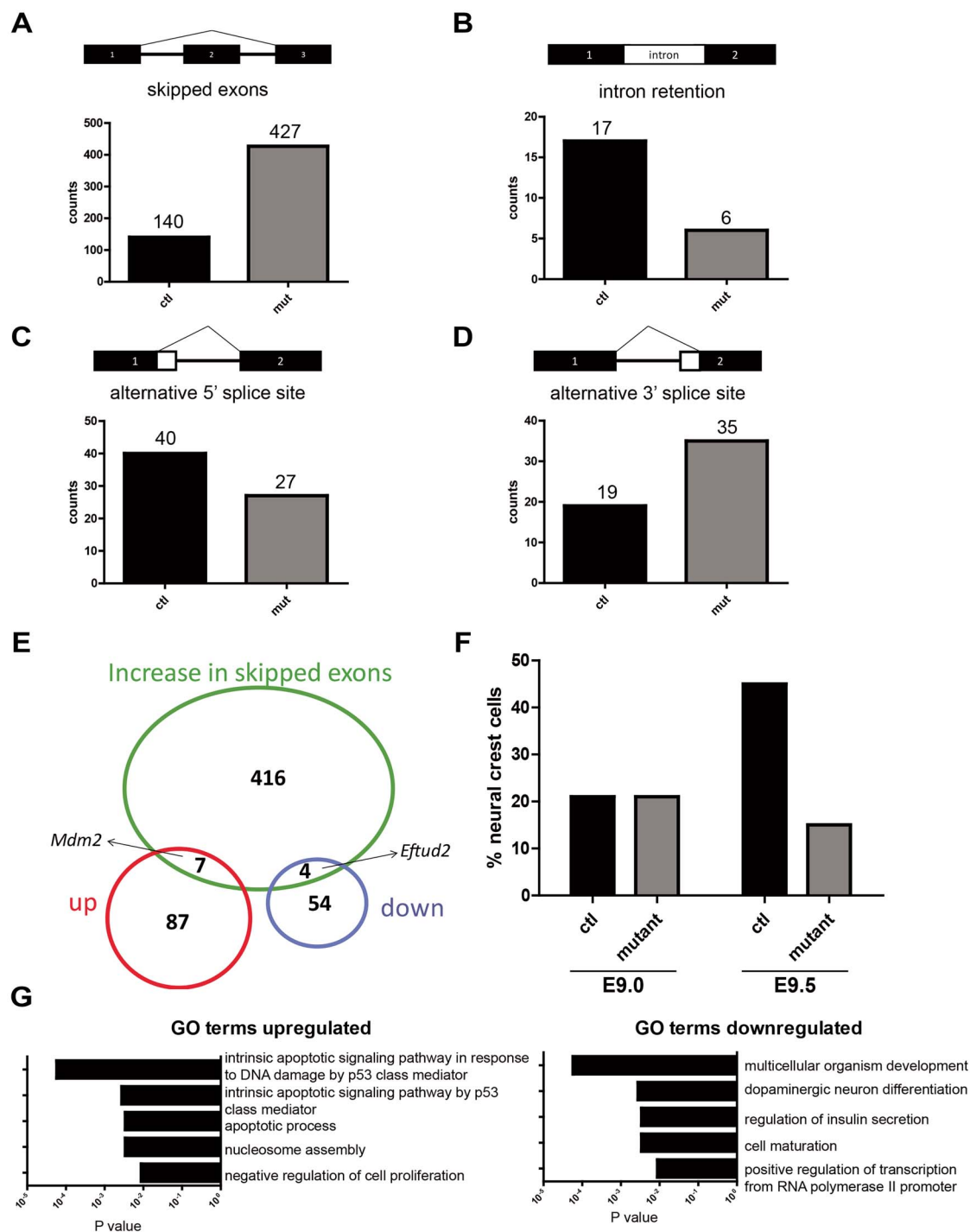


Figure 5. RNAseq analysis at E9.0 reveals increased exon skipping and upregulation of the P53 pathway. The number of various alternative splicing events is represented and a sign test performed to compare the tendency for each type of event to occur preferentially in mutants versus controls (A) skipped exons ($P < 0.0001$) (B) intron retention ($P < 0.05$, more frequent in controls) (C) alternative 5' splice site (D) alternative 3' splice site ($P < 0.05$ when jointly testing 5' and 3' splice site preference for the usage of downstream site). (E) Venn Diagram showing genes with skipped exons in mutant embryos that were also upregulated (including *Mdm2*) or downregulated (including *Eftud2*) (F) The percentage of neural crest cells in heads of control and mutant embryos at E9.0 and E9.5 using the exclusion of exon 2 of *Eftud2* from the RNAseq data as a surrogate for the neural crest cells population (see Materials and Methods). (G) GO terms analysis of genes that were upregulated or downregulated in mutant versus controls.

neural crest cell-specific *Eftud2* homozygous mutant embryos, the alternative splicing events found did not correlate with a significant overall change in gene expression. Thus, our results do not support the role of mutant EFTUD2-associated splicing

defects in downregulation of gene expression through PTC inclusion.

To determine if splicing is also altered in patient derived cells, we compared results of RNAseq analysis of lymphoblastoid

B-cell lines (LCL) from four unrelated MFDM patients to one control. We identified 35 common splicing changes in these cell lines that were not seen in the control (3 3'SS; 6 5'SS; 21 SE; 5 MXE; [Supplementary Material, Tables S3 and S4](#)). While this analysis was underpowered and the transcriptome of immortalized LCLs is not likely a relevant model for human neural crest cells in MFDM, the existence of recurrent splicing changes in these human models supports a mechanism of MFDM involving splicing changes.

Genes in the P53—pathway are upregulated in *Eftud2* mutant neural crest cells

We next analyzed our data set to identify genes upregulated and downregulated in the heads of neural crest cell-specific *Eftud2* homozygous mutant embryos. At E9.0, 94 transcripts were upregulated and 58 transcripts were downregulated in mutants when compared with controls ([Fig. 5E](#)). An analysis of gene ontology terms significantly associated with these transcripts revealed the two most significant upregulated pathways to be intrinsic apoptotic signalling pathway in response to DNA damage by P53 class mediator and intrinsic apoptotic signalling pathway by P53 class mediator ([Fig. 5G](#)). The two most significant downregulated pathways were multicellular organism development and dopaminergic neuron differentiation ([Fig. 5G](#)). A comparable analysis using KEGG revealed P53 signalling to be the most significantly upregulated pathway (data not shown). Similarly, the P53-signalling pathway was among the top pathways significantly upregulated in LCLs from MFDM patients ([Supplementary Material, Table S5](#)).

Using RT-qPCR, we confirmed significant increases of P53—pathway genes: *Ccng1*, *Phlda3*, *Trp53inp1* and *Mdm2*, in the head of neural crest cell-specific *Eftud2* homozygous mutant embryos ([Fig. 6A](#)). To test if reduced levels of *Eftud2* in neural crest cells also led to increased levels of P53 target genes, we transfected mouse neural crest cells from line O9-1 with an *Eftud2* siRNA to reduce levels of this gene. RT-qPCR revealed that expression of *Ccng1*, *Phlda3* and *Trp53inp1* were also significantly increased in cells with *Eftud2* knockdown when compared with controls ([Supplementary Material, Fig. S7](#)). These data indicate that reducing levels of *Eftud2* results in increased P53 activity.

Mutations of *Eftud2* lead to increased skipping of exon 3 of *Mdm2*, a master regulator of P53, and an increase in nuclear P53

Though a global change in gene expression was not associated with the alternative splicing events found in neural crest cell-specific *Eftud2* homozygous mutant embryos, our data confirmed increased skipping of the deleted exon 2 in *Eftud2* which was associated with downregulated expression of this gene ([Fig. 5E](#)). The list of genes with increased alternative splicing also included increased skipping of exon 3 of *Mdm2*, the master regulator of P53 ([Fig. 5E](#)). Alternative splicing of exon 3 of *Mdm2* produces a shorter protein that can no longer bind to MDM4 and leads to stabilization and upregulation of P53 (32). Therefore, we used RT-PCR to examine alternative splicing of this gene in E9.0 embryos. Using primers targeting exon 2 and 6 of *Mdm2*, the proportion of *Mdm2* transcripts lacking exon 3 was found to be significantly increased in *Eftud2* homozygous neural crest mutant embryos when compared with controls ([Fig. 6B](#)). Similarly, O9-1 neural crest cells with knockdown of *Eftud2* ([Fig. 6C](#)) also showed a significant increase in *Mdm2* transcripts

lacking exon 3 when compared with controls. We used exon-specific primers in the 5' exon of human *MDM2* to analyze splicing of this gene in patient LCLs. We found a significant reduction in transcripts containing *MDM2* exon 2, indicating it is this exon that is more often skipped in these patient LCLs ([Fig. 6D](#)). To assess if the increased splicing of *Mdm2* exon 3 was responsible for the overactivation of the p53 pathway in neural crest cells, we overexpressed full-length *Mdm2* in cells transfected with *Eftud2* siRNA and evaluated splicing of *Mdm2* and expression of *Ccng1*, *Phlda3* and *Trp53inp1*. No difference was found in splicing of *Mdm2* when full-length *Mdm2* was overexpressed ([Fig. 6C](#)). But, as shown in [Figure 6E](#), although not significant, there was a tendency towards decreased expression of all genes in the p53 pathway in cells with *Mdm2* overexpression.

Increased skipping of exon 3 of *Mdm2* was also previously shown to lead to increased nuclear P53 (33). To determine if this is the case in mutant embryos, we performed immunohistochemistry to detect P53 in E9.0 mutant ($n=4$) and control ($n=5$) embryos. P53 was barely detectable in control embryos, while striking expression of nuclear P53 was found in the neuroepithelium and surrounding head mesenchyme of all E9.0 neural crest cell-specific *Eftud2* homozygous mutant embryos ([Fig. 6F](#)). These findings indicate that reduced levels of *Eftud2* leads to alternative splicing of *Mdm2*, and that this in turn results in increased accumulation of nuclear P53 and expression of P53 target genes.

Decreasing P53 activity with Pifithrin- α rescues a subset of craniofacial defects in *Eftud2* neural crest mutants

Our data show that neural crest cells with mutation of *Eftud2* have increased P53 activity and consequently fail to survive and/or expand. Therefore, we postulated that reducing P53 activity could protect these cells from death and rescue morphological abnormalities found in neural crest cell-specific *Eftud2* homozygous mutant embryos. Pifithrin- α is a reversible chemical inhibitor of P53 that is thought to protect cells from P53-induced cell death by decreasing nuclear P53 activity or modulating its nuclear import/export (28). Jones and colleagues showed that craniofacial malformations could be prevented in *Tcof1* heterozygous mutant embryos with increased levels of P53 when treated in utero with pifithrin- α (34). To test if craniofacial defects in neural crest-specific *Eftud2* homozygous mutant embryos could be prevented, we treated pregnant females with pifithrin- α or DMSO/PBS (vehicle) daily starting at E6.5 until E8.5 and collected embryos at E9.5. We first evaluated midbrain development. As shown in [Figure 7A](#), control embryos treated with vehicle ($n=8/8$) or pifithrin- α ($n=12/12$) showed normal midbrain development (highlighted in green and data not shown). On the other hand, a subset of neural crest cell-specific *Eftud2* homozygous mutant embryos treated with pifithrin- α showed a significant improvement in midbrain development ($n=3/11$) when compared with vehicle and untreated mutant embryos ($n=0/41$; $P=0.0139$, Fisher's exact test). We next evaluated the perimeter of the first pharyngeal arch (black dotted lines) of the same groups of embryos ([Fig. 7A](#)). Treatment with pifithrin- α did not impact the perimeter of pharyngeal arch 1 of control embryos, however, pifithrin- α treatment significantly increased the size of the first pharyngeal arch in neural crest cell-specific *Eftud2* homozygous mutant embryos, $P < 0.05$ by t-test ([Fig. 7B](#)). Taken together, these data show for the first time that the P53 inhibitor pifithrin- α can, at least partly,

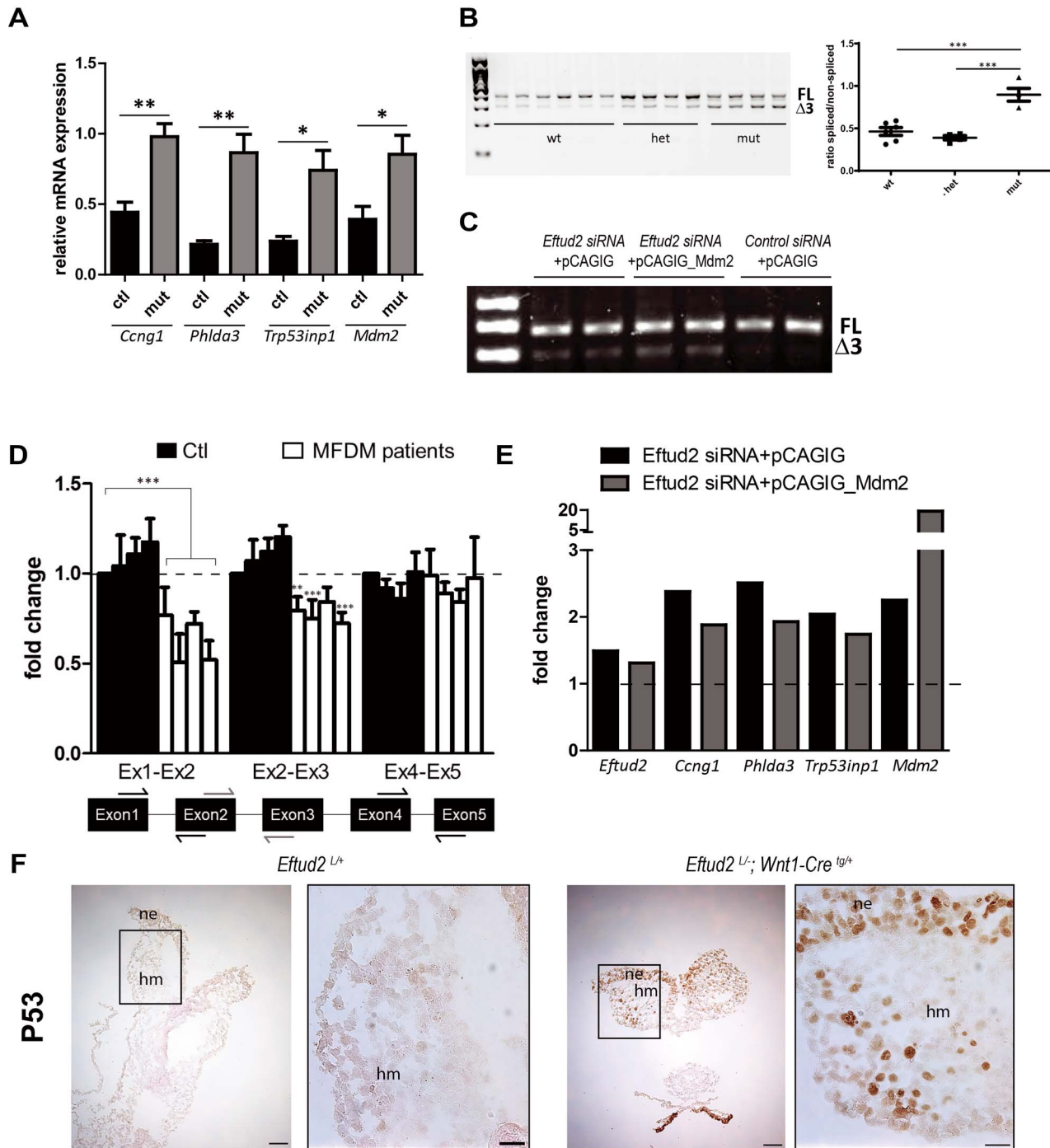


Figure 6. Alternatively spliced and overexpressed *Mdm2* leads to increased p53 when *Eftud2* is mutated. (A) RT-qPCR showing increased expression of P53 target genes in E9.0 *Eftud2*^{loxP/-}; *Wnt1-cre*^{tg/+} mutant embryos ($n = 3$) compared with control embryos ($n = 3$). Samples were assayed in duplicates and are described in [Supplementary Material, Table S6](#). * $P < 0.05$ ** $P < 0.01$ by t-test. (B) RT-PCR using primers flanking exon 3 of *Mdm2* confirms a significant increase in transcripts with skipped *Mdm2* exon 3 in E9.0 *Eftud2*^{loxP/-}; *Wnt1-cre*^{tg/+} mutant embryos. Left, representative gel image and right, quantification of splicing of *Mdm2* exon 3. *** $P < 0.001$ by t-test. FL: full-length transcript Δ 3: transcript without exon 3. (C) Representative RT-PCR using the same primers for *Mdm2* in O9-1 cells showing increase of the *Mdm2* transcript with skipped exon 3 in cells transfected with *Eftud2* siRNA (with empty pCAGIG or *Mdm2*-pCAGIG vector) compared with control siRNA with empty pCAGIG vector. (D) RT-qPCR showing fold change of *Mdm2* transcripts with exons 1–4 in LCL lines isolated from MFDM patients when compared with controls. Schematic highlights primer flanking locations. P-values calculated from $\Delta\Delta$ Ct levels (ANOVA). Mean values with SEM error bars are shown ($n = 3$). (E) Fold change in *Eftud2*, *Ccng1*, *Trp53inp1*, *Phlda3* and *Mdm2* levels in O9-1 neural crest cells transfected with *Eftud2* siRNA and pCAGIG (black bars) or pCAGIG_Mdm2 (gray bars) expression vectors. Dashed horizontal lines denote expression in control cells transfected with pCAGIG. Data presented as average fold-change. (F) Representative image of sections of E9.0 control (*Eftud2*^{loxP/+}) and *Eftud2*^{loxP/-}; *Wnt1-cre*^{tg/+} mutant embryos showing increased P53 (brown) positive cells after IHC. ne: neuroepithelium, hm: head mesenchyme. Scale bars, lower magnification = 75 μ m, higher magnification = 25 μ m.

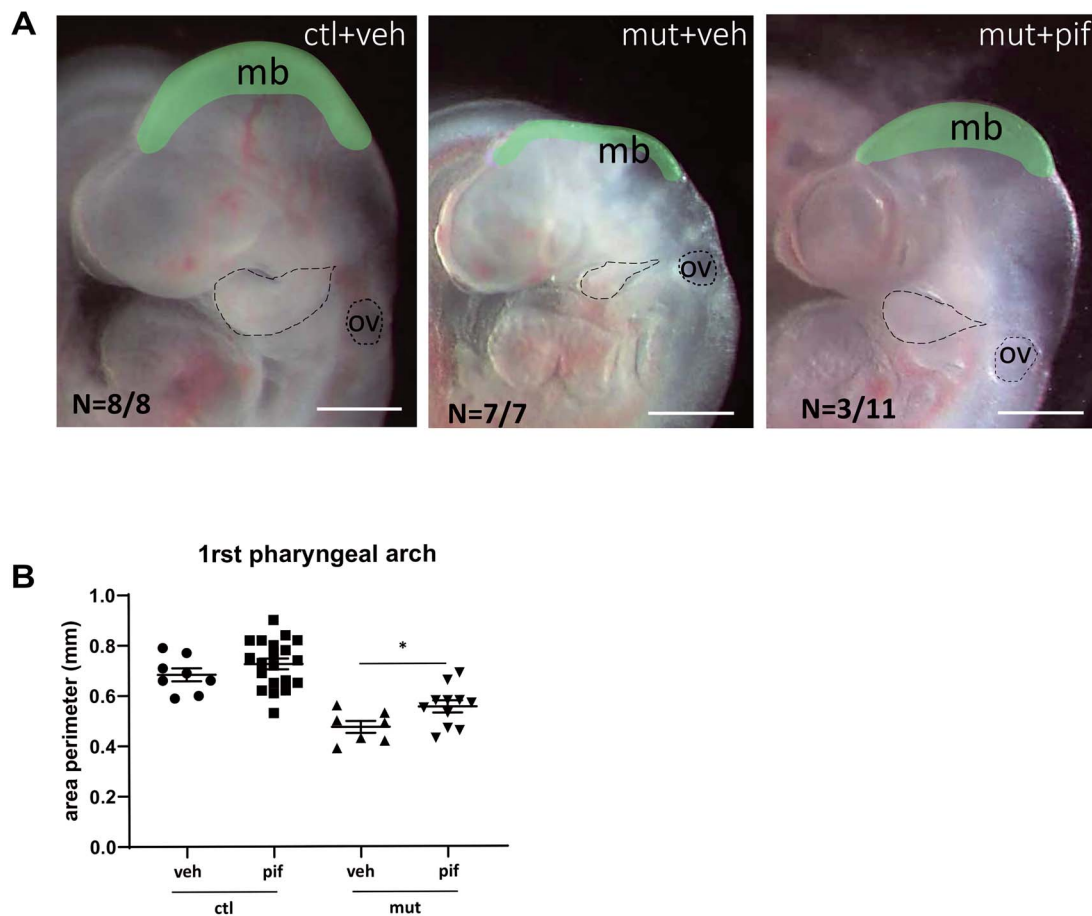


Figure 7. Pifithrin- α partially rescues craniofacial abnormalities in *Eftud2*^{loxP/-}; *Wnt1-cre*^{tg/+} mutant embryos. Pregnant females were treated daily with vehicle (veh:2% DMSO/PBS; $n = 3$) or 2.2 mg/kg pifithrin- α (pif) ($n = 7$) I.P. for 3 days from E6.5 to E8.5, and embryos were collected at E9.5. (A) Representative pictures of control embryos (*Eftud2*^{loxP/+} and *Eftud2*^{loxP/+}; *Wnt1-cre*^{tg/+}) treated with vehicle (ctl + veh), neural crest mutant embryos (*Eftud2*^{loxP/-}; *Wnt1-cre*^{tg/+}) treated with vehicle (mut + veh), and neural crest mutant embryos treated with pifithrin- α (mut + pif). The latest were categorized by their head morphology (green area) as normal, $n = 3/11$ or abnormal, $n = 8/11$. (B) Perimeter of first left pharyngeal arches (black dotted lines). * $P < 0.05$ by t-test. Scale bar = 500 μm .

prevent craniofacial abnormalities in a mouse model carrying mutation in *Eftud2*.

Discussion

Haploinsufficiency of *EFTUD2* was first reported in 2012 to be the cause of MFDM (12). Patients with MFDM exhibit a variety of clinical findings and the most common are craniofacial defects such as microcephaly, developmental delay, mandibular and malar hypoplasia as well as external ear anomalies. In addition, as no correlation is found between patient's genotypes and their clinical characteristics, these mutations are predicted to be loss-of-function mutations and suggest that the developing craniofacial region is more sensitive to reduced levels of *EFTUD2* when compared with other embryonic cell types (reviewed in (7)). Here, we report that altered splicing caused by the loss of *Eftud2* results in the reduced inclusion of exon 3 of *Mdm2* and nuclear accumulation of P53 in the mutant neural crest cells. Though we cannot rule out that cell-cycle arrest contributes to

loss of neural crest cells at E9.0, our data suggest that P53 activation triggers cell death by E9.5 thus leading to a decrease in the number of neural crest cells that can contribute to craniofacial development. Our findings provide a mechanistic link between *EFTUD2* splicing and MFDM. We hypothesize that variability in the number of surviving neural crest cells is responsible for the range of clinical findings reported in MFDM patients.

Mutations of *Eftud2* in neural crest cells model MFDM

A number of animal models carrying *Eftud2* mutations have been reported in zebrafish and in mouse (17,25–27). Three zebrafish models targeted the *eftud2* gene in different ways: one TALEN-derived deletion in the fifth exon, c.378_385, disrupts part of the GTP binding domain (17), a 5 bp deletion in exon 2 also generated using TALEN mutates part of the N-acidic terminal domain (27) and an N-ethyl-N-nitrosourea (ENU) induced nonsense C-T mutation in exon 24 of *eftud2* mutates part of the conserved EF 2 domain IV (26). These mutants were all predicted or shown to have a decrease or absence of *eftud2* protein. Interestingly,

all the homozygous mutant zebrafish embryos exhibited similar phenotypes: smaller head size, smaller eyes, curved body tail and embryonic lethality while heterozygous mutants were normal. A shortened jawbone and deformity of Meckel's cartilage was found in heterozygous fish with mutation of the N-acidic terminal domain (27).

We reported a unique mouse model with heterozygous *Eftud2* mutation in which exon 2, part of the N-terminal acidic region, was deleted, and led to the generation of an unstable protein (25). In an outbred genetic background, heterozygous mice were viable and fertile and showed no major phenotypic abnormalities whereas homozygous mutants arrested pre-implantation (25). However, although heterozygous pups on the inbred C57Bl/6 genetic background showed no obvious craniofacial malformations, a small but significant number of these pups were lost between birth and weaning. The mouse model described herein is the first to show craniofacial defects similar to those found in patients with mutations in *EFTUD2*, suggesting that the cell of origin of *Eftud2*-associated craniofacial defects is the neural crest cells. Neural crest cells contribute extensively to the formation of the bones of the face and skull (35), forming mostly the anterior part of the head (36).

Over 90% of MFDM patients have defects in derivatives of the frontonasal prominence and first arch that are consistent with abnormal neural crest cell formation and/or differentiation. Nonetheless, a substantial number of patients show abnormalities consistent with abnormal development of structures that are derived from cranial neural crest cells that populate pharyngeal arches 2–5, as well as cardiac neural crest cells (37). Similarly, in neural crest cell-specific *Eftud2* homozygous mutant embryos, structures formed from the cranial neural crest cells that colonize the frontonasal prominence as well as the pharyngeal arches are affected. In addition, our data suggest that *Eftud2* is also required in cardiac neural crest cells, suggesting that congenital heart abnormalities such as truncus arteriosus and ventricular septal defects, reported in a subset of MFDM patients (37,38), are due to a requirement for *EFTUD2* in these cells. The reduced size and abnormal shape of the bony labyrinth of the inner ear of neural crest-specific *Eftud2* homozygous mutant embryos are unlikely to be due to a cell-autonomous requirement for *Eftud2* in the neural crest. In fact, though neural crest cells provide signals for differentiation of glia of the cochleovestibular ganglion, and differentiate to form melanocytes of the stria vascularis, and hair cells (39), they do not contribute to the bony labyrinth. Thus, additional studies are needed to explain the specific requirement for *Eftud2* in inner ear development.

Splicing defects in *Eftud2* mutant models are associated with increased P53 activity

EFTUD2 is a core component of the U5 spliceosome complex that binds to the 5' (upstream) and 3' (downstream) exons during the two splicing steps. U5 binds the 5' exons intermediate generated after the first splicing reaction to tether and align it to the 3' exons for the second step of the splicing reaction (40). GTP-bound *EFTUD2* is predicted to activate the RNA helicase involved in the first step of splicing (41) and formation of the lariat intron intermediate. Additionally, dephosphorylation of *EFTUD2* is predicted to contribute to spliceosome disassembly (42,43). However, recent crystal structures of the pre- and post-catalytic spliceosome suggest that *EFTUD2* interaction with PRP8 may predominantly serve as a 'relay station' which enables efficient splicing (44).

RNA sequencing analysis of zebrafish with a mutation in the fifth exon of *eftud2* revealed a transcriptome-wide RNA splicing deficiency. These mutants had a large number of transcripts with increased intron-retention and exon-skipping, leading to overwhelming nonsense-mediated RNA decay (26). The increased stress on the non-sense mediated pathway was predicted to activate P53 and result in apoptosis (26). Although a partial rescue of mutant phenotypes and apoptosis was observed when a key gene in the nonsense-mediated pathway, *upf1*, was overexpressed (26) or when p53 was inhibited by morpholinos in two different mutant models (26,27), no direct link was made between splicing and P53 activation.

Recently, Wood et al. reported RNA-seq results in induced pluripotent and induced neural crest cells derived from a single Burn-McKeown (BMK) Syndrome patient with bi-allelic mutation in *TXNL4*, another core component of the U5 spliceosome. Although reduced *TXNL4* levels were associated with reduced proliferation and a significant increase in skipped exons in both cell lines, stress response pathways including P53 and ER-stress were not upregulated (45). In contrast, a loss-of-function heterozygous mutation in *EFTUD2* in the human embryonic kidney cell line HEK293K, lead to reduced *EFTUD2* protein levels, a decrease in proliferation and increased sensitivity to endoplasmic reticulum (ER) stress (46). Interestingly, RNA sequencing analysis revealed widespread changes in expression of a number of genes, as well as general splicing differences, most of which were skipped exons. They proposed that the observed splicing differences may indicate 'mis-splicing' which could lead to an overwhelming burden of unfolded proteins in the ER, ultimately inducing apoptosis. Similarly, experiments aimed at evaluating the role of *EFTUD2* on human osteoblast proliferation showed that *EFTUD2* knockdown in HCO (human calvarial osteoblast) and in HC-a (human articular chondrocyte) cells reduced their proliferation and differentiation (27). Again, RNA sequencing uncovered that the P53 pathway was the most severely affected. It is not clear why a stress response was not found in *TXNL4* mutant cells considering the significant increase in abnormal splicing reported. Furthermore, though BMKS and MFDM patients share a subset of phenotypic defects including mandibular hypoplasia, the protein encoded by these two genes have distinct temporal requirement in the U5 snRNP. *TXNL4A* is removed when the activated catalytic complex form, while *EFTUD2* is required until the intron lariat is removed (3). Thus, it is not surprising that the set of genes with abnormal increase in skipped exons in *EFTUD2* mutant cells were not shared in *TXNL4A* mutant cells. However, the fact that different cell types were analyzed in each of these studies may be the major reason that genes with skipped exons in *TXNL4* mutant cells were distinct from those found in cells with reduced levels of *EFTUD2* (45,46).

Our study also shows that there is a significant increase in exon skipping in heads of *Eftud2* neural crest cell mutant embryos as compared with controls. However, other alternative splicing events are more difficult to interpret. At E9.0, we do observe a slight tendency towards higher intron retention in the mutants, which is consistent with observations made in other model systems; however, this trend is not seen at E9.5. Other events, such as alternative 5' and 3' splice site usage and mutually exclusive exons also do not show consistent trends across stages. It is likely that our system has limited power to detect the less frequent types of splicing defects, since we estimate that mutant neural crest cell constitute only a fraction of the tissue profiled by RNA-seq. Focusing on the most consistent and abundant category—exon skipping events—we asked whether

there is any tendency towards inefficient recognition of weak splice sites in the mutants, but we did not observe any difference between splice site strength of exons with decreased, as compared with increased inclusion. This observation is consistent with the function of EFTUD2 as a GTP-ase and its involvement in maintaining splicing efficiency, but not the recognition of the splice site signals. Contrary to previous hypotheses, we did not find global disruption in expression of genes that contained differential splicing events predicted to lead to premature termination and subject to non-sense-mediated decay. Furthermore, we did not find significant changes in expression of genes important for nonsense mediated decay (data not shown) or upregulation of this pathway. Instead, our data revealed an enrichment of an alternatively spliced *Mdm2* transcript, that was previously shown to lead to P53-stabilization and increased P53 activity (32). Similar changes in *Mdm2* splicing were also found in the O9-1 neural crest cell line. Although exonic and intronic organization of human and mouse *Mdm2* is not conserved, the protein sequences encoded in Exon 3 of mouse *Mdm2* is nearly identical to that encoded in Exon 2 of human *MDM2* (Supplementary Material, Fig. S8). Hence, we postulate that this splicing change is the key event which leads to increased P53 activity in mammalian cells.

Increased P53 activity and neural crest cell death are responsible for craniofacial malformations in the *Eftud2*; *Wnt1-Cre2* mutant mouse model

Genes in the P53 pathway that are upregulated in *Eftud2* mutant neural crest cells, such as *Ccng1*, *Phlda3* and *Trp53inp1* are important executors in cell cycle arrest and apoptosis. *Ccng1* encodes for Cyclin G1 and was first identified as a P53 transcriptional target (47). It is involved in P53 stabilization in response to DNA-damage and regulates G2/M arrest in a p53-dependent manner (48). *Phlda3* encodes for Pleckstrin Homology Like Domain Family A Member 3 and is a P53-regulated repressor of Akt (49). *Trp53inp1* encodes for Tumor protein p53-inducible nuclear protein 1, an antiproliferative and proapoptotic protein involved in cell stress response that acts as an antioxidant and plays a major role in p53-driven oxidative stress response (50). Expression of these genes are likely responsible for the death of *Eftud2* mutant neural crest cells and the profound disruption of craniofacial cartilage formation by E14.5. Pifithrin- α is thought to protect cells from P53-induced cell death by decreasing nuclear P53 activity or modulating its nuclear import/export (28). Genetically mutant embryos with morphological abnormalities that were rescued by pifithrin- α had reduced levels of P53, its target genes, like *Ccng1*, and apoptosis (34,51,52). However, we did not find significant reduction in P53-pathway genes in neural crest cell-specific *Eftud2* homozygous mutant embryos treated with pifithrin- α (data not shown). Hence, genetic studies using P53 mutant mice and longer treatment with pifithrin are needed to determine if improved craniofacial development is the result of reduced cell death.

The question of phenotypic variability most likely reflects the quantity and/or developmental timepoint at which these cells die. Hence, in embryos where the majority of neural crest cells die before differentiation, structures are likely to be absent, like we found for Meckel's cartilage, while death of a lesser number of these cells would lead to hypoplasia and/or malformed cartilages and bones. This is supported by our work with pifithrin- α which indicates that decreasing P53 activity leads to almost normal morphogenesis of the midbrain and improves the size of the pharyngeal arches. However, as many transcripts

were misregulated in these mutant embryos, it remains to be determined how far development can be pushed and if a similar increase in P53 activity contributes to craniofacial defects that are associated with mutations in other splicing factors.

Our current working model is that mutations which reduce levels of EFTUD2 lead to increased exclusion of exon 3 of *Mdm2*. We think that this splicing event directly or indirectly leads to activation of P53. P53 is an established stress response pathway, which provides a cell suffering from stress a chance to correct the error, in this case, a reduction in spliceosome activity. In the absence of an efficient response, the cells are then eliminated via cell death. Thus, mutant neural crest cells can be generated, migrate, colonize and differentiate in the developing craniofacial region. Determining whether MFDM clinical abnormalities would be alleviated solely by modulating P53 signaling, with the cancer risks it poses, or in combinations with other strategies to restore the other developmental networks that are surely also disrupted in these patients, will be of great importance.

Materials and Methods

Mouse lines

All procedures and experiments were performed according to the guidelines of the Canadian Council on Animal Care and approved by the Animal Care Committee of the Montreal Children's Hospital. Wild-type CD1 mice were purchased from Charles Rivers (strain code 022) and wild-type C57Bl/6 mice were purchased from Jackson Laboratories (stock #000664). The R26R strain (Gt(ROSA)26Sor^{tm1Sor} stock #003309 from Jackson's Lab) was a kind gift from Dr Nagano. These mutant mice carry a loxP flanked DNA STOP sequence upstream preventing expression of the downstream *lacZ* gene. When crossed with a *cre* transgenic strain, the STOP sequence is removed and *lacZ* is expressed in *cre*-expressing tissues (53). *Wnt1-Cre2* mice were purchased from Jackson's laboratory (stock #022137). These *Wnt1-Cre2* transgenic mice express Cre recombinase under the control of the mouse *Wnt1*, wingless-related MMTV integration site 1, promoter and enhancer (29).

Generation of *Eftud2* mouse line using CRISPR/Cas9 gene-editing system

gRNAs and microinjections for the CRISPR/Cas9 strategy used to generate the conditional mutant *Eftud2* line were described previously (25). Briefly, two single stranded DNA template (ssDNA: custom-made from IDT) containing loxP sequences, EcoR1 and EcoRV flanking exon 2 of *Eftud2* were purchased. On a first round of micro-injection using gRNAs 1–4 and both ssDNA templates, one female with EcoR1/loxP insertion in the intron upstream of exon 2 was recovered. She was mated to a wild-type C57/Bl6 male and one of her male offspring with Sanger-sequenced verified insertion of the EcoR1/loxP template was used for another round of micro-injection with gRNAs 3 and 4 and the EcoRV/loxP ssDNA targeting the intron downstream of exon 2. From this second round of injections, 1 male and 1 female with EcoR1 and EcoR5 digest products were identified. Both were mated with wild-type CD1 mice to generate G1. Intact loxP sequences were Sanger-sequenced verified in the G1 offspring of the founder male (Supplementary Material, Fig. S9). Thereafter, a G1 female carrying sequence-verified loxP sequences flanking exon 2 of *Eftud2* was backcrossed to wild-type CD1 or wild-type C57BL/6 mice for 5 generations to establish the *Eftud2* conditional mutant mouse. Embryos generated from

mating of heterozygous mice from the fifth generation onwards were analyzed in this study. *Eftud2*^{loxP/+} mice were mated with each other to obtain *Eftud2*^{loxP/loxP}.

Generation of neural crest cell-specific deletion mutation in *Eftud2*

We first introduced the *Wnt1-Cre2* transgene in constitutive *Eftud2*^{+/-} mice to obtain *Eftud2*^{+/-}; *Wnt1-Cre2*^{tg/+}. These mice were then mated with mice carrying conditional loxP mutations: *Eftud2*^{loxP/loxP}. The embryos obtained (*Eftud2*^{loxP/-}; *Wnt1-Cre2*^{tg/+}) have homozygous *Eftud2* mutation in neural crest cells and heterozygous *Eftud2* mutation in all other cells. Alternatively, we also mated *Wnt1-Cre2*^{tg/+} mice with *Eftud2*^{loxP/+} to obtain *Eftud2*^{loxP/+}; *Wnt1-Cre2*^{tg/+}. These mice were then mated with mice carrying conditional loxP mutations: *Eftud2*^{loxP/loxP}. The embryos obtained (*Eftud2*^{loxP/loxP}; *Wnt1-Cre2*^{tg/+}) have homozygous *Eftud2* mutation in neural crest cells and are wild-type in all other cells.

Genotyping of mice

Genomic DNA was extracted from mouse tails or yolk sacs as previously described (54). For *Eftud2*, genotyping was performed using 3-primers targeting exon 2 of *Eftud2* using the following program: 30 s 95°C, 30 s 55°C, 30 s 72°C for 35 cycles followed by an elongation step of 10 min at 72°C. As depicted in [Supplementary Material, Figure S9](#), the PCR condition was optimized to amplify a wild-type (180 bp), a mutant (265 bp) and a conditional *Eftud2* (214 bp) amplicon. The following primers were used: *Eftud2* F1: atgaaccaggcgagagaagt, *Eftud2* R1: tccaacagtagccaagc-cat, *Eftud2* R2: ccatgatgctaaaattcaaggag. For the commercially available lines, namely *Wnt1-Cre2* and R26R, genotyping was conducted as detailed on Jackson's laboratory website: protocol #29915 (R26R) and #25394 (*Wnt1-Cre2*).

Collection of embryos

For embryo collection, the day of the presence of vaginal plug was considered embryonic day 0.5 (E0.5). Embryos were collected and yolk sacs were used for genomic DNA extraction for genotyping. For stages E8.5–E10.5, the number of somites were counted under light microscope (Leica MZ6 Infinity1 stereomicroscope) at the time of dissection. Embryos were fixed in 4% paraformaldehyde at 4°C overnight (unless otherwise stated), washed in PBS and kept at 4°C.

Cartilage preparation

To evaluate cartilage formation, embryos were stained with Alcian Blue as previously described (55). Briefly, E14.5 embryos were fixed in Bouin's fixing solution for 2 h followed by several washes in 70% ethanol. Embryos were then stain in an Alcian blue staining solution (0.03% Alcian blue in 80% ethanol; 20% acetic acid) for 24–48 h at 37°C. Finally, embryos were cleared in BABB (benzyl alcohol: benzyl benzoate, 1:2) solution and visualized under light microscope (Leica MZ6 Infinity1 stereomicroscope).

Probe production

For Sox10 probe, the plasmid was a kind gift from Dr Trainor (34). Briefly, it was linearized with BamH1 and transcribed using T3 polymerase or linearized with EcoR1 and transcribed with T7 polymerase to generate the sense and antisense probes,

respectively. Transcription of probes was done using the DIG RNA Labeling Mix (Roche). All protocols were used according to the manufacturer's instructions.

Preparation of embryos for in-situ hybridization, embedding and histology

Dissected embryos were fixed in 4% paraformaldehyde overnight and dehydrated using a graded methanol series for whole-mounts. Wholemount in situs were performed as previously described (56). For morphological analysis, E14.5 and E17.5 embryos were first decalcified in 10% EDTA for 2 weeks, then dehydrated and embedded in paraffin. Ten micrometer sections were performed on a Leica RM 2155 microtome and mounted on coated slide for further staining with hematoxylin and eosin. For cryo-embedding, fixed embryos were first cryoprotected in 30% sucrose overnight and sectioned at 10 µm thickness for IF and IHC.

Wholemount β-galactosidase staining

Embryos were fixed in 0.4% paraformaldehyde for approximately 45 min, washed in detergent rinse solution (0.02% Igepal, 0.01% sodium deoxycholate, 2 mM MgCl₂ in 0.1 M phosphate buffer pH 7.5) 3 times 15 min and stain by immersion in freshly prepared 1 mg/ml X-gal staining solution (0.02% Igepal, 0.01% Sodium Deoxycholate, 5 mM Potassium Ferricyanide, 5 mM Potassium Ferrocyanide and 2 mM MgCl₂ in 0.1 M phosphate buffer pH 7.5) overnight at 37°C in the dark. Embryos were washed in PBS and post-fix in 4% paraformaldehyde in PBS at 4°C overnight. For sectioning, embryos were embedded in Sheldon Cryomatrix (Thermoscientific) before storage in –80°C.

Wholemount immunohistochemistry

Embryos were fixed in 0.4% PFA overnight at 4°C, washed and dehydrated in increasing concentration of methanol and kept at –20°C until use. Staining was performed as previously described (57). Briefly, after rehydration in PBS, embryos were bleached ON in methanol:DMSO:H₂O₂ (4:1:1) solution. They were incubated with 2H3 (DHSB 1:150) and with mouse HRP-secondary antibody (1:500) and developed with DAB. Embryos were then visualized under light microscope (Leica MZ6 Infinity1 stereomicroscope).

Immunofluorescence and TUNEL assay

Immunofluorescence experiments were performed according to standard protocols (68). The following primary antibodies were used: Phosphohistone H3 (Ser10; 1:200 dilution, Millipore, 06–570). Alexa Fluor 568 (ThermoFisher, 1:500 dilutions) secondary antibody was used. For the quantification of apoptosis, the In Situ Cell Death Detection Kit, TMR red was used (Roche, cat# 12156792910) and manufacturer's protocol was followed. Slides were mounted with VECTASHIELD hard-set mounting medium with DAPI to visualize the nuclei. Images were captured on a Leicamicrosystem (model DM6000B) and Leica camera (model DFC 450). For quantification of fluorescence signal, particle analysis on Image J was used.

O9-1 cell culture

O9-1 cells were cultured and maintained as described (58). LIF (HY-P7084), b-FGF (HY-P7004) and Mitomycin C (HY-13316) were purchased from MedChem Express. The only deviation from the protocol consisted of collecting conditioned basal O9-1 media

from STO cells over the course of 5 days. All cells used for experimentation had passage numbers less than 7 and were passaged at least twice before any given experiment. Cells were cultured in 24-well plates for all experiments.

Transfection of O9-1 cells with siRNAs

O9-1 cells were cultured to be 40–60% confluent on the day of transfection. *Eftud2* and negative control siRNAs (5 pmol) were transfected using the Lipofectamine[®] RNAiMAX transfection kit following the manufacturer's protocol and recommendations. The cells were rinsed in cold 1X PBS and collected in 500 µl of TRIzol reagent (cat# 15596026, Thermo Fischer Scientific) 36 h post-transfection. RNA was extracted following the manufacturer's protocol and recommendations. For the rescue experiment, 7.5 h after the above mentioned transfection, the cells were transfected with 1.5 µg pCAGIG or pCAGIG_Mdm2. pCAGIG was a gift from Connie Cepko (59) (Addgene plasmid #11159; <http://n2t.net/addgene:11159>; RRID: Addgene11159). To generate pCAGIG_Mdm2, the coding sequence of *Mdm2* (consisting of exons 3 through 12) was amplified with the following primers: F: GTTAGACAAAACCATTCGCTTT and R: CTAGTTGAAGTAAGTTAGCACAATCA using the Q5[®] High-Fidelity DNA Polymerase and Q5[®] Reaction Buffer and cloned into the *EcoRV* site of pCAGIG. The cells were incubated for 36 h after transfection with the pDNAs and RNA was extracted as described above. RT-qPCRs in O9-1 cells were performed in three technical replicates using two biological replicates.

Annexin V cell death assay

O9-1 cells were cultured in 24-well plates to be 50–60% confluent on the day of transfection. *Eftud2* and negative control siRNAs were transfected using Lipofectamine[®] RNAiMAX as described previously. The cells were incubated in a 37°C humidified incubator (5% CO₂) for 24 h post-transfection. Following the PBS wash, the cells were washed twice with 1X AnnexinV binding buffer (cat# V13246, Thermo Fischer Scientific). The AnnexinV staining solution (cat# A13201, Thermo Fisher Scientific) was added and incubated in the dark, for 15 min. Fluorescence was measured using a microplate reader with Ex: 495 nm, ex: 519 nm.

RNA isolation for RNA sequencing and RT-qPCR

RNA extraction from samples described in [Supplementary Material, Tables S6 and S7](#) was performed using Qiagen RNeasy kit following manufacturer's protocol. An aliquot was sent for RNA sequencing analysis. Total RNA was treated with DNase (NEB, according to manufacturer's protocol) and used for reverse transcription with the iScript[™] cDNA synthesis kit (Bio-rad, cat#170-8890, according to the manufacturer's protocol). qRT-PCR was performed using the ssoAdvanced universal SYBR green supermix (Bio-Rad, cat#172-5270) on a Roche LightCycle 480 PCR machine. qPCR experiments were performed in duplicates to ensure technical replicability. Target genes were normalized with the normalization factor as calculated by geNorm software (v3.4; Ghent university hospital center for medical genetics) (60). Three house-keeping genes including *B2M*, *GAPDH* and *SDHA* were used for generation of the normalization factor as previously reported (60). RT-PCR program included a hot start at 95°C for 5 min, followed by 40 cycles of a denaturation step at 95°C for 10 s and an annealing/extension step at 60°C for 30 s. Primers used are listed in [Supplementary Material, Table S8](#).

RNA sequencing

Sequencing libraries were prepared by Genome Quebec Innovation Centre (Montreal, Canada), using the TruSeq Stranded Total RNA Sample Preparation Kit (Illumina TS-122-2301, San Diego, CA, USA) by depleting ribosomal and fragmented RNA, synthesizing first and second strand cDNA, adenylating the 3' ends and ligating adaptors, and enriching the adaptor-containing cDNA strands by PCR. The libraries were sequenced using the Illumina HiSeq 4000 PE100 sequencer, 100 nucleotide paired-end reads, generating approximately between 31 and 63 million reads sample. The sequencing reads were trimmed using CutAdapt (61) and mapped to the mouse reference genome (mm10) using STAR (62) aligner (version 2.4.0e), with default parameters, and annotated using the Gencode (63) M2 (version M2, 2013) annotation. Htseq-count (part of the 'HTSeq' (64) framework, version 0.5.4p5.) was used for expression quantification.

To perform a differential splicing analysis, we used rMATS 4.0.2 (65). To determine if there is a difference in skipping exons between heterozygous and homozygous samples, we used the Skipped Exon events reported by rMATS. The events that had a mean of inclusion junction counts (IJC) and a mean of skipped junction counts (SJC) lower than 10 in homozygous or heterozygous samples were removed from the analysis. We used the inclusion level supplied by rMATS as a difference between the average of inclusion level in heterozygous samples and the average of inclusion level in homozygous samples. We computed the number of events with an inclusion level difference more than 0.1 or less than -0.1, and a nominal P-value < 0.05 (uncorrected for multiple testing). The rationale for not using FDR correction is to obtain a large dataset enriched for alternative splicing in order to observe general tendencies, such as for example increased propensity for exon skipping or intron retention in the mutants.

To further explore intron retention events, we used IRFinder (31) with default settings and a nominal P-value < 0.05, again motivated by the goal to detect general trends in splicing changes.

We used DESeq2 (66) for differential expression analysis. Genes with a mean of read counts less or equal to 10 in homozygous and heterozygous samples were removed from the analysis. A gene set list of interest was then derived by applying filters on gene expression, such that only those with P-adj < 0.05 and FoldChange > 0 and P-adj < 0.05 and FoldChange < 0 were selected as up- and down-regulated genes.

A DAVID (version 6.8) (67) pathway analysis was performed using the list of up- and down-regulated genes. The genes used for differential expression analysis were used as background.

Using RNA-seq data to estimate the proportion of neural crest cells

We represent the total amount of *Eftud2* Transcripts observed in the control samples as

$$T_{oc} = Nm(1 - p) + \frac{Nmp(1 + s)}{2}$$

where N is the total number of cells, m is the number of transcripts produced per cell, p is the proportion of neural crest cells in the head region and s is the relative stability of the *Eftud2dExon2* product, which is expected to introduce a frameshift and may be less stable than the complete mRNA. The first term in the equation represents transcripts obtained from normal cells (wt), and the second-term transcripts from the

neural crest fraction (which are *wt/Eftud2dExon2*). To determine the proportion of normal *Eftud2* transcripts, which is equivalent to the percent-spliced-in (PSI) value for inclusion of exon 2 estimated by rMATS, we find:

$$\text{PSI}_c = \frac{T_{oc(n)}}{T_{oc}} = \left(Nm(1-p) + \frac{Nmp}{2} \right) / T_{oc}$$

And rearranging

$$1 - \text{PSI}_c = \frac{p}{2} (1 - \text{PSI}_c (1 - s))$$

Similarly, for the mutant embryos, where the non-neural crest cells are (*wt/Eftud2dExon2*) and neural crest cells are (*Eftud2DExon2/Eftud2DExon2*).

$$1 - \text{PSI}_m = p(1 - \text{PSI}_m) + s\text{PSI}_m(1 + p)$$

At E9.0, before the occurrence of any phenotypic defects, we assume that the proportion of neural crest cells (p) is the same in mutant and control embryos, and the relative stability (s) of the mutant *Eftud2* product is a constant parameter to be estimated. The PSI values in control and mutants estimated by rMATS are ($\text{PSI}_c = 0.93; \text{PSI}_m = 0.51$), and the above two simultaneous equations can be solved for s and p . Because of the non-linear (sp) term the solutions are quadratic, but only one set of solutions ($s = 0.65; x = 0.21$) corresponds to physiologically relevant parameters.

At E9.5, when phenotypic defects become apparent, we can use the corresponding PSI values ($\text{PSI}_c = 0.84; \text{PSI}_m = 0.53$) and the relative stability value ($s = 0.65$) determined above to estimate the proportion of neural crest cells separately in control (p_c) and mutant embryos (p_m) and show that, while this proportion increases in the controls ($p_c = 0.45$), it is further reduced in the mutants ($p_m = 0.15$).

Primers used for splicing analysis

For *Mdm2* splicing analysis, cDNA was amplified with a RT-PCR program that included a hot start at 95°C for 5 min, followed by 35 cycles of a denaturation step at 95°C for 10 s and an annealing step at 55°C for 30 s, an extension step at 72°C for 45 s with a final extension step at 72°C for 10 min, and visualized on a 2% agarose gel. The primers used are as follow: Forward (exon2–6/7): GATCACCGCGCTTCTCCTGC, Reverse (exon2–6/7): GATGTGCCA-GAGTCTTGCTG (33).

Immunohistochemistry

P53 primary antibody was used (1:250, cat#2524, Cell Signaling) and the VECTASTAIN® Universal Quick HRP Kit (PK-8800, Vector Laboratories) was used as secondary antibody and visualized with DAB (Vector Laboratories). After rinsing with water, slides were mounted with an aqueous mounting medium and images were captured on a Leicamicrosystem (model DM6000B) and Leica camera (model DFC 450).

LCL RNA isolation for RNA sequencing and RT-qPCR

Patient cell lines were obtained from the Care4Rare Canada Consortium with informed consent (Protocol 11/04E; Research Ethics Board of the Children's Hospital of Eastern Ontario;

Supplementary Material, Table S3). Total RNA from WT and MFDM patient derived lymphoblastoid cell lines (LCL) was isolated using RNeasy Plus Mini Kit (Qiagen, Cat. #74134) following manufacturer's protocol. An aliquot was sent for RNA sequencing analysis. For RT-qPCR, RNA from LCLs was reverse transcribed to cDNA using Transcriptor First Strand cDNA Synthesis Kit (Roche, Cat. #04896866001). RT-qPCR was performed in triplicate using Fast SYBR Green Master Mix (ThermoFisher Scientific, Cat. #4385612) and StepOnePlus Real-Time PCR system (Applied Biosystems). Primers used are listed in Supplementary Material, Table S8.

LCL RNA sequencing

Library construction was performed on total RNA ($\text{RIN} \geq 9.0$ assessed with Agilent 6000 Nano analysis, Agilent Technologies), using pipeline for poly(A)-selected/ribo-depleted strand-specific mRNA-seq library construction from the Michael Smith Genome Sciences Centre. Biological triplicates or duplicates (Supplementary Material, Table S3) of RNA from each cell line were sequenced on a HiSeq 2500 (Illumina) using 75 bp paired-end sequencing.

Pifithrin- α treatment

Pregnant females were injected with 2.2 mg/mg pifithrin- α , as previously described (34), or 2% DMSO/PBS (vehicle) daily through intra-peritoneal injection, starting at E6.5 until E8.5 and collected embryos at E9.5.

Statistical analysis

Two-tailed unpaired t-test analysis was calculated using Excel and Prism Software and Chi-square test was calculated using Prism. Significant P-values are represented as * $P < 0.05$, ** $P < 0.01$ and *** $P < 0.001$.

All unique/stable reagents generated in this study are available from the Lead Contact with a completed Materials Transfer Agreement.

Supplementary Material

Supplementary Material is available at HMG online.

Acknowledgments

We would like to thank Dr Mitra Cowan, Associate Director of the transgenic core facility at McGill University, Goodman Cancer Center, for the micro-injections experiments. We thank the patients who agreed to participate in the study. We would like to thank all members of the Jerome-Majewska lab for their invaluable input in the writing of the manuscript.

Conflict of Interest statement. The authors declare no competing interests.

Funding

Care4Rare Canada Consortium funded by Genome Canada and the Ontario Genomics Institute (OGI-147), the Canadian Institutes of Health Research, Ontario Research Fund, Genome Alberta, Genome British Columbia, Genome Quebec and Children's Hospital of Eastern Ontario Foundation (to K.M.B. and M.A.L.); NIH (grant 2R15DE026611-02 to J.L.F.); the Canadian

Institutes of Health Research (MOP#142452 to L.J.A.-M. and J.M.); L.J.A.-M. and J.M. are members of the Research Centre of the McGill University Health Centre which is supported in part by Fonds de Recherche Santé Québec.

Author's Contribution

M.-C.B. carried out and analyzed all of the mouse experiments, drafted the manuscript and designed the figures. A.D. and E.B. performed the data analysis from the RNAseq experiments. F.M. carried out and analyzed all the mouse neural crest cell line experiments. R.A. performed IHC experiments and part of the cartilage analysis. A.S.T. did the experiments using the patients cell lines. K.M.B., M.A.L. recruited patients involved in the study. P.C.S. supervised the analysis of experiments using patients cell lines. J.L.F. supervised the analysis of experiments using the O9-1 mouse neural crest cell line. J.M. supervised all bioinformatics analysis from the RNAseq. J.M. and L.A.J.-M. devised the project. L.A.J.-M. conceptualized and supervised all the mouse experiments, and wrote the manuscript. All authors provided critical feedback and helped shape the research, analysis and manuscript.

References

- Papasaïkas, P. and Valcarcel, J. (2016) The spliceosome: the ultimate RNA chaperone and sculptor. *Trends Biochem. Sci.*, **41**, 33–45.
- Sperling, R. (2017) The nuts and bolts of the endogenous spliceosome. Wiley interdisciplinary reviews. RNA, **8**, e1377.
- Will, C.L. and Luhrmann, R. (2011) Spliceosome structure and function. *Cold Spring Harb. Perspect. Biol.*, **3**, a003707.
- Wickramasinghe, V.O., González-Porta, M., Perera, D., Bartolozzi, A.R., Sibley, C.R., Hallegger, M., Ule, J., Marioni, J.C. and Venkitaraman, A.R. (2015) Regulation of constitutive and alternative mRNA splicing across the human transcriptome by PRPF8 is determined by 5' splice site strength. *Genome Biol.*, **16**, 201.
- Olthof, A.M., Hyatt, K.C. and Kanadia, R.N. (2019) Minor intron splicing revisited: identification of new minor intron-containing genes and tissue-dependent retention and alternative splicing of minor introns. *BMC Genomics*, **20**, 686.
- Will, C.L., Schneider, C., Hossbach, M., Urlaub, H., Rauhut, R., Elbashir, S., Tuschl, T. and Luhrmann, R. (2004) The human 18S U11/U12 snRNP contains a set of novel proteins not found in the U2-dependent spliceosome. *RNA (New York, NY)*, **10**, 929–941.
- Beauchamp, M.C., Alam, S.S., Kumar, S. and Jerome-Majewska, L.A. (2020) Spliceosomopathies and neurocrisopathies: two sides of the same coin? *Dev. Dyn.*, in press. doi: 10.1002/dvdy.183.
- Daguenet, E., Dujardin, G. and Valcarcel, J. (2015) The pathogenicity of splicing defects: mechanistic insights into pre-mRNA processing inform novel therapeutic approaches. *EMBO Rep.*, **16**, 1640–1655.
- Griffin, C. and Saint-Jeannet, J.P. (2020) Spliceosomopathies: diseases and mechanisms. *Dev. Dyn.*, in press. doi: 10.1002/dvdy.214.
- Lehalle, D., Wiczorek, D., Zechi-Ceide, R.M., Passos-Bueno, M.R., Lyonnet, S., Amiel, J. and Gordon, C.T. (2015) A review of craniofacial disorders caused by spliceosomal defects. *Clin. Genet.*, **88**, 405–415.
- Gordon, C.T., Petit, F., Oufadem, M., Decaestecker, C., Jourdain, A.S., Andrieux, J., Malan, V., Alessandri, J.L., Baujat, G., Baumann, C. et al. (2012) EFTUD2 haploinsufficiency leads to syndromic oesophageal atresia. *J. Med. Genet.*, **49**, 737–746.
- Lines, M.A., Huang, L., Schwartzentruber, J., Douglas, S.L., Lynch, D.C., Beaulieu, C., Guion-Almeida, M.L., Zechi-Ceide, R.M., Gener, B., Gillessen-Kaesbach, G. et al. (2012) Haploinsufficiency of a spliceosomal GTPase encoded by EFTUD2 causes mandibulofacial dysostosis with microcephaly. *Am. J. Hum. Genet.*, **90**, 369–377.
- Czeschik, J.C., Voigt, C., Alanay, Y., Albrecht, B., Avci, S., Fitzpatrick, D., Goudie, D.R., Hehr, U., Hoogeboom, A.J., Kayserili, H. et al. (2013) Clinical and mutation data in 12 patients with the clinical diagnosis of Nager syndrome. *Hum. Genet.*, **132**, 885–898.
- Luquetti, D.V., Hing, A.V., Rieder, M.J., Nickerson, D.A., Turner, E.H., Smith, J., Park, S. and Cunningham, M.L. (2013) Mandibulofacial dysostosis with microcephaly caused by EFTUD2 mutations: expanding the phenotype. *Am. J. Med. Genet. A*, **161a**, 108–113.
- Voigt, C., Megarbane, A., Neveling, K., Czeschik, J.C., Albrecht, B., Callewaert, B., von Deimling, F., Hehr, A., Falkenberg Smeland, M., König, R. et al. (2013) Oto-facial syndrome and esophageal atresia, intellectual disability and zygomatic anomalies—expanding the phenotypes associated with EFTUD2 mutations. *Orphanet J. Rare Dis.*, **8**, 110.
- Lehalle, D., Gordon, C.T., Oufadem, M., Goudefroye, G., Boutaud, L., Alessandri, J.L., Baena, N., Baujat, G., Baumann, C., Boute-Benejean, O. et al. (2014) Delineation of EFTUD2 haploinsufficiency-related phenotypes through a series of 36 patients. *Hum. Mutat.*, **35**, 478–485.
- Deml, B., Reis, L.M., Muheisen, S., Bick, D. and Semina, E.V. (2015) EFTUD2 deficiency in vertebrates: identification of a novel human mutation and generation of a zebrafish model. *Birth Defects Res. A Clin. Mol. Teratol.*, **103**, 630–640.
- Sarkar, A., Emrick, L.T., Smith, E.M., Austin, E.G., Yang, Y., Hunter, J.V., Scaglia, F. and Lalani, S.R. (2015) Novel de novo mutations in EFTUD2 detected by exome sequencing in mandibulofacial dysostosis with microcephaly syndrome. *Am. J. Med. Genet. A*, **167a**, 914–918.
- Smigiel, R., Bezniakow, N., Jakubiak, A., Bloch, M., Patkowski, D., Obersztyn, E. and Sasiadek, M.M. (2015) Phenotype analysis of polish patients with mandibulofacial dysostosis type Guion-Almeida associated with esophageal atresia and choanal atresia caused by EFTUD2 gene mutations. *J. Appl. Genet.*, **56**, 199–204.
- Zarate, Y.A., Bell, C. and Schaefer, G.B. (2015) Radioulnar synostosis and brain abnormalities in a patient with 17q21.31 microdeletion involving EFTUD2. *Cleft Palate Craniofac. J.*, **52**, 237–239.
- Huang, L., Vanstone, M.R., Hartley, T., Osmond, M., Barrowman, N., Allanson, J., Baker, L., Dabir, T.A., Dipple, K.M., Dobyns, W.B. et al. (2016) Mandibulofacial dysostosis with microcephaly: mutation and database update. *Hum. Mutat.*, **37**, 148–154.
- Matsuo, M., Yamauchi, A., Ito, Y., Sakauchi, M., Yamamoto, T., Okamoto, N., Tsurusaki, Y., Miyake, N., Matsumoto, N. and Saito, K. (2017) Mandibulofacial dysostosis with microcephaly: a case presenting with seizures. *Brain Dev.*, **39**, 177–181.
- Rengasamy Venugopalan, S., Farrow, E.G. and Lypka, M. (2017) Whole-exome sequencing identified a variant in EFTUD2 gene in establishing a genetic diagnosis. *Orthod. Craniofac. Res.*, **20**, 50–56.
- Yu, K.P.T., Luk, H.M., Gordon, C.T., Fung, G., Oufadem, M., Garcia-Barcelo, M.M., Amiel, J., Chung, B.H.Y., Lo, I.F.M. and

- Tiong, Y.T. (2018) Mandibulofacial dysostosis Guion-Almeida type caused by novel EFTUD2 splice site variants in two Asian children. *Clin. Dysmorphol.*, **27**, 31–35.
25. Beauchamp, M.C., Djedid, A., Daupin, K., Clokie, K., Kumar, S., Majewski, J. and Jerome-Majewska, L.A. (2019) Loss of function mutation of Eftud2, the gene responsible for mandibulofacial dysostosis with microcephaly (MFDm), leads to pre-implantation arrest in mouse. *PLoS One*, **14**, e0219280.
 26. Lei, L., Yan, S.Y., Yang, R., Chen, J.Y., Li, Y., Bu, Y., Chang, N., Zhou, Q., Zhu, X., Li, C.Y. et al. (2017) Spliceosomal protein eftud2 mutation leads to p53-dependent apoptosis in zebrafish neural progenitors. *Nucleic Acids Res.*, **45**, 3422–3436.
 27. Wu, J., Yang, Y., He, Y., Li, Q., Wang, X., Sun, C., Wang, L., An, Y. and Luo, F. (2019) EFTUD2 gene deficiency disrupts osteoblast maturation and inhibits chondrocyte differentiation via activation of the p53 signaling pathway. *Hum. Genomics*, **13**, 63.
 28. Komarov, P.G., Komarova, E.A., Kondratov, R.V., Christov-Tselkov, K., Coon, J.S., Chernov, M.V. and Gudkov, A.V. (1999) A chemical inhibitor of p53 that protects mice from the side effects of cancer therapy. *Science (New York, NY)*, **285**, 1733–1737.
 29. Lewis, A.E., Vasudevan, H.N., O'Neill, A.K., Soriano, P. and Bush, J.O. (2013) The widely used Wnt1-Cre transgene causes developmental phenotypes by ectopic activation of Wnt signaling. *Dev. Biol.*, **379**, 229–234.
 30. Fan, X., Loebel, D.A., Bildsoe, H., Wilkie, E.E., Qin, J., Wang, J. and Tam, P.P. (2016) Tissue interactions, cell signaling and transcriptional control in the cranial mesoderm during craniofacial development. *AIMS Genet.*, **3**, 74–98.
 31. Middleton, R., Gao, D., Thomas, A., Singh, B., Au, A., Wong, J.J., Bomane, A., Cosson, B., Eyra, E., Rasko, J.E. et al. (2017) IRFinder: assessing the impact of intron retention on mammalian gene expression. *Genome Biol.*, **18**, 51.
 32. Giglio, S., Mancini, F., Pellegrino, M., Di Conza, G., Puxeddu, E., Sacchi, A., Pontecorvi, A. and Moretti, F. (2010) Regulation of MDM4 (MDMX) function by p76(MDM2): a new facet in the control of p53 activity. *Oncogene*, **29**, 5935–5945.
 33. Van Alstyne, M., Simon, C.M., Sardi, S.P., Shihabuddin, L.S., Mentis, G.Z. and Pellizzoni, L. (2018) Dysregulation of Mdm2 and Mdm4 alternative splicing underlies motor neuron death in spinal muscular atrophy. *Genes Dev.*, **32**, 1045–1059.
 34. Jones, N.C., Lynn, M.L., Gaudenz, K., Sakai, D., Aoto, K., Rey, J.P., Glynn, E.F., Ellington, L., Du, C., Dixon, J. et al. (2008) Prevention of the neurocristopathy Treacher Collins syndrome through inhibition of p53 function. *Nat. Med.*, **14**, 125–133.
 35. Gilbert, S.F. (2010) *Developmental Biology*, 9th edn. Sinauer, Sunderland, MA.
 36. McBratney-Owen, B., Iseki, S., Bamforth, S.D., Olsen, B.R. and Morriss-Kay, G.M. (2008) Development and tissue origins of the mammalian cranial base. *Dev. Biol.*, **322**, 121–132.
 37. Abell, K., Hopkin, R.J., Bender, P.L., Jackson, F., Smallwood, K., Sullivan, B., Stottmann, R.W., Saal, H.M. and Weaver, K.N. (2020) Mandibulofacial dysostosis with microcephaly: An expansion of the phenotype via parental survey. *Am. J. Med. Genet. A*, in press. doi: [10.1002/ajmg.a.61977](https://doi.org/10.1002/ajmg.a.61977).
 38. Chapnik, E., Sasson, V., Belloch, R. and Hornstein, E. (2012) Dgcr8 controls neural crest cells survival in cardiovascular development. *Dev. Biol.*, **362**, 50–56.
 39. Ritter, K.E. and Martin, D.M. (2019) Neural crest contributions to the ear: implications for congenital hearing disorders. *Hear. Res.*, **376**, 22–32.
 40. Newman, A.J. (1997) The role of U5 snRNP in pre-mRNA splicing. *EMBO J.*, **16**, 5797–5800.
 41. Brenner, T.J. and Guthrie, C. (2006) Assembly of Snu114 into U5 snRNP requires Prp8 and a functional GTPase domain. *RNA (New York, NY)*, **12**, 862–871.
 42. Agafonov, D.E., Kastner, B., Dybkov, O., Hofele, R.V., Liu, W.T., Urlaub, H., Luhrmann, R. and Stark, H. (2016) Molecular architecture of the human U4/U6.U5 tri-snRNP. *Science (New York, NY)*, **351**, 1416–1420.
 43. Frazer, L.N., Nancollis, V. and O'Keefe, R.T. (2008) The role of Snu114p during pre-mRNA splicing. *Biochem. Soc. Trans.*, **36**, 551–553.
 44. Jia, J., Ganichkin, O.M., Preußner, M., Absmeier, E., Alings, C., Loll, B., Heyd, F. and Wahl, M.C. (2020) A Snu114-GTP-Prp8 module forms a relay station for efficient splicing in yeast. *Nucleic Acids Res.*, **48**, 4572–4584.
 45. Wood, K.A., Rowlands, C.F., Thomas, H.B., Woods, S., O'Flaherty, J., Douzou, S., Kimber, S.J., Newman, W.G. and O'Keefe, R.T. (2020) Modelling the developmental spliceosomal craniofacial disorder burn-McKeown syndrome using induced pluripotent stem cells. *PLoS One*, **15**, e0233582.
 46. Wood, K.A., Rowlands, C.F., Qureshi, W.M.S., Thomas, H.B., Buczek, W.A., Briggs, T.A., Hubbard, S.J., Hentges, K.E., Newman, W.G. and O'Keefe, R.T. (2019) Disease modeling of core pre-mRNA splicing factor haploinsufficiency. *Hum. Mol. Genet.*, **28**, 3704–3723.
 47. Okamoto, K. and Beach, D. (1994) Cyclin G is a transcriptional target of the p53 tumor suppressor protein. *EMBO J.*, **13**, 4816–4822.
 48. Kimura, S.H. and Nojima, H. (2002) Cyclin G1 associates with MDM2 and regulates accumulation and degradation of p53 protein. *Genes Cells*, **7**, 869–880.
 49. Kawase, T., Ohki, R., Shibata, T., Tsutsumi, S., Kamimura, N., Inazawa, J., Ohta, T., Ichikawa, H., Aburatani, H., Tashiro, F. et al. (2009) PH domain-only protein PHLDA3 is a p53-regulated repressor of Akt. *Cell*, **136**, 535–550.
 50. Cano, C.E., Gommeaux, J., Pietri, S., Culcasi, M., Garcia, S., Seux, M., Barelier, S., Vasseur, S., Spoto, R.P., Pébusque, M.J. et al. (2009) Tumor protein 53-induced nuclear protein 1 is a major mediator of p53 antioxidant function. *Cancer Res.*, **69**, 219–226.
 51. Morgan, S.C., Lee, H.Y., Relaix, F., Sandell, L.L., Levorse, J.M. and Loeken, M.R. (2008) Cardiac outflow tract septation failure in Pax3-deficient embryos is due to p53-dependent regulation of migrating cardiac neural crest. *Mech. Dev.*, **125**, 757–767.
 52. Pani, L., Horal, M. and Loeken, M.R. (2002) Rescue of neural tube defects in Pax-3-deficient embryos by p53 loss of function: implications for Pax-3-dependent development and tumorigenesis. *Genes Dev.*, **16**, 676–680.
 53. Soriano, P. (1999) Generalized lacZ expression with the ROSA26 Cre reporter strain. *Nat. Genet.*, **21**, 70–71.
 54. Hou, W., Gupta, S., Beauchamp, M.C., Yuan, L. and Jerome-Majewska, L.A. (2017) Non-alcoholic fatty liver disease in mice with heterozygous mutation in TMED2. *PLoS One*, **12**, e0182995.
 55. Rigueur, D. and Lyons, K.M. (2014) *Skeletal Development and Repair*. Springer, pp. 113–121.
 56. Revil, T. and Jerome-Majewska, L.A. (2013) During embryogenesis, esrp1 expression is restricted to a subset of epithelial cells and is associated with splicing of a number of developmentally important genes. *Dev. Dyn.*, **242**, 281–290.

57. Jerome-Majewska, L.A., Achkar, T., Luo, L., Lupu, F. and Lacy, E. (2010) The trafficking protein Tmed2/p24beta(1) is required for morphogenesis of the mouse embryo and placenta. *Dev. Biol.*, **341**, 154–166.
58. Nguyen, B.H., Ishii, M., Maxson, R.E. and Wang, J. (2018) Culturing and manipulation of O9-1 neural crest cells. *JoVE*. doi: [10.3791/58346](https://doi.org/10.3791/58346).
59. Matsuda, T. and Cepko, C.L. (2004) Electroporation and RNA interference in the rodent retina in vivo and in vitro. *Proc. Natl. Acad. Sci. USA*, **101**, 16–22.
60. Vandesompele, J., De Preter, K., Pattyn, F., Poppe, B., Van Roy, N., De Paepe, A. and Speleman, F. (2002) Accurate normalization of real-time quantitative RT-PCR data by geometric averaging of multiple internal control genes. *Genome Biol.*, **3**, 1–0034.11.
61. Martin, M. (2011) Cutadapt removes adapter sequences from high-throughput sequencing reads. *EMBnet. J.*, **17**, 10–12.
62. Dobin, A., Davis, C.A., Schlesinger, F., Drenkow, J., Zaleski, C., Jha, S., Batut, P., Chaisson, M. and Gingeras, T.R. (2013) STAR: ultrafast universal RNA-seq aligner. *Bioinformatics (Oxford, England)*, **29**, 15–21.
63. Mudge, J.M. and Harrow, J. (2015) Creating reference gene annotation for the mouse C57BL6/J genome assembly. *Mamm. Genome*, **26**, 366–378.
64. Anders, S., Pyl, P.T. and Huber, W. (2015) HTSeq—a python framework to work with high-throughput sequencing data. *Bioinformatics (Oxford, England)*, **31**, 166–169.
65. Shen, S., Park, J.W., Lu, Z.X., Lin, L., Henry, M.D., Wu, Y.N., Zhou, Q. and Xing, Y. (2014) rMATS: robust and flexible detection of differential alternative splicing from replicate RNA-Seq data. *Proc. Natl. Acad. Sci. USA*, **111**, E5593–E5601.
66. Love, M.I., Huber, W. and Anders, S. (2014) Moderated estimation of fold change and dispersion for RNA-seq data with DESeq2. *Genome Biol.*, **15**, 550.
67. Huang, D.W., Sherman, B.T., Tan, Q., Collins, J.R., Alvord, W.G., Roayaei, J., Stephens, R., Baseler, M.W., Lane, H.C. and Lempicki, R.A. (2007) The DAVID gene functional classification tool: a novel biological module-centric algorithm to functionally analyze large gene lists. *Genome Biol.*, **8**, R183.
68. Zakariyah, A., Hou, W., Slim, R. and Jerome-Majewska, L. (2011) TMED2/p24β1 is expressed in all gestational stages of human placentas and in choriocarcinoma cell lines. *Placenta*, **33** (3), 214–219.